FLOW AND TEMPERATURE FIELDS GENERATED BY A THERMALLY ACTIVATED INTERVENTIONAL VASCULAR DEVICE

A Thesis

by

CASEY DAVID MCCURRIN

Submitted to the Office of Graduate Studies of
Texas A&M University
in partial fulfillment of the requirements for the degree of

MASTER OF SCIENCE

August 2012

Major Subject: Biomedical Engineering

Flow and Temperature Fields Generated by a Thermally

Activated Interventional Vascular Device

FLOW AND TEMPERATURE FIELDS GENERATED BY A THERMALLY ACTIVATED INTERVENTIONAL VASCULAR DEVICE

A Thesis

by

CASEY DAVID MCCURRIN

Submitted to the Office of Graduate Studies of
Texas A&M University
in partial fulfillment of the requirements for the degree of

MASTER OF SCIENCE

Approved by:

Chair of Committee,	Duncan J. Maitland
Committee Members,	James E. Moore, Jr.
	Jim Ji
Head of Department,	Gerard Cote

August 2012

Major Subject: Biomedical Engineering

ABSTRACT

Flow and Temperature Fields Generated by a Thermally Activated Interventional Vascular Device. (August 2012)

Casey David McCurrin, B.S., Texas A&M University

Chair of Advisory Committee: Dr. Duncan J. Maitland

Concern for the nonphysiologic energy required to actuate medical devices utilizing "smart material" properties of shape memory polymer (SMP) compels a rigorous investigation into the flow and temperature fields surrounding a thermally activated catheter device. Multiple analyses include the theoretical approaches of exact analytical solutions and finite difference modeling combined with the experimental techniques of particle image velocimetry (PIV) and laser-induced fluorescence (LIF). The attained velocities and temperatures related to the convective heat transfer impact the potential for blood or tissue damage caused by intravascular heating.

The clinical scenario involving a catheter device receiving heat within an artery is modeled in its simplest form as a cylindrical metal cap on the tip of a hollow glass rod placed inside of a long straight tube of constant cross-sectional area. Using a working fluid with properties comparable to blood, flow rates and energy input is then varied to determine their effects on velocity fields and temperature gradients.

Analytical solutions for both the straight tube and concentric annulus demonstrate the two velocity distributions involved, as flow moves past the gap between

the catheter and artery wall and then converges downstream to the Poiseuille solution for steady pipe flow of an incompressible fluid. To solve for the transition between the velocity profiles, computational fluid dynamics software simulates a finite volume model identical to the experimental setup used for intravascular heating experiments.

PIV and LIF, both experimental techniques making use of similar hardware, determine velocity fields and temperature distributions, respectively, by imaging fluid seeding agents and their particular interaction with the light sheet. The velocity and temperature fields obtained experimentally are matched with the analytical and finite volume analysis through fluid properties, flow rates, and heating rates.

Velocities determined during device heating show a small increase in local velocity, due to temperature dependent viscosity effects. When the device is centered in the model, flow patterns constrain the heat flow near the center axis and away from the channel walls. Increasing flow rate consequently decreases temperature rise, as the heat is carried more quickly downstream and away from the heat source.

Using multiple analyses, fluid velocity and temperature distributions are first theorized with analytical and finite element methods and then validated through experimental imaging in a physical model.

ACKNOWLEDGMENTS

I would like to thank my committee chair, Dr. Maitland, for giving me the opportunity to expand my horizons in the ever-growing realm of biomedical research. His guidance and insight have been crucial to this study.

Thanks to all my wonderful lab mates who have helped me cross the necessary hurdles to get here. Without Wonjun Hwang's endless knowledge of all things mechanical, John Horn's skillful device manufacturing, or Edward Hahn's modeling and PIV experience, I never would have made it.

Thanks also to my fellow Aggies, whether friends, classmates, faculty, or staff of the biomedical engineering department, for making the most out of my time at Texas A&M University. You make me proud to bleed maroon and white.

Thanks to my mother and father for putting me in a position to win, providing countless advantages and opportunities while letting me choose my own path, and for their continued support and encouragement, both psychologically and financially.

Finally, I wish to acknowledge NIH/NIBIB grant R01EB000462 for the funding used to support this work.

NOMENCLATURE

PIV	Particle Image Velocimetry
LIF	Laser-Induced Fluorescence
CFD	Computational Fluid Dynamics
SMP	Shape Memory Polymer
BMF	Blood Mimicking Fluid
PDMS	Polydimethylsiloxane

Re	Reynolds number $= u_m D_h/\nu$
Pr	Prandtl number $= \nu/\alpha$
Nu	Nusselt number $= hD_h/k$
Pe	Peclet number $= Re \cdot Pr$

ρ	density	$\left[\frac{g}{cm^3}\right]$
μ	kinematic viscosity	$\left[\frac{g}{cm \cdot s}\right]$ = [Poise]
ν	dynamic viscosity $= \frac{\mu}{\rho}$	$\left[\frac{cm^2}{s}\right]$
k	thermal conductivity	$\left[\frac{W}{mK}\right]$
C_p	specific heat capacity	$\left[\frac{J}{gK}\right]$
α	thermal diffusivity $= \frac{k}{\rho C_p}$	$\left[\frac{m^2}{s}\right]$

r	radius	[cm]
u	axial velocity component	$\left[\frac{m^2}{s}\right]$
A_c	cross-sectional area	[cm^2]
D_h	hydraulic diameter for pipe $= D = 2r_o$	[cm]
	hydraulic diameter for annulus $= D_h = 2(r_o - r_i)$	[cm]
P	hydrostatic pressure	[Pa]
Q	mean volumetric flow rate	$\left[\frac{mL}{min}\right]$
q"	heat flux $= \frac{q}{A_c}$	$\left[\frac{W}{cm^2}\right]$
T	temperature	[°C]

$r*$	annulus ratio $= \frac{r_i}{ro}$
$\bar{r}$	normalized radius $= \frac{r}{r_o}$
$\bar{u}$	normalized velocity $= \frac{u}{u_m}$
x^*	dimensionless axial coordinate $= \frac{x/D_h}{Re \cdot Pr}$
B	constant $= \frac{r^{*2}-1}{\ln r^*}$
M	constant $= 1 + r^{*2} - B$
θ_i	normalized temperature (at inner wall) $= \frac{T-T_e}{q_i"\left(\frac{D_h}{k}\right)}$

Subscripts

e	entrance
fd	fully developed
i	inner surface
o	outer surface
j	heated surface
k	opposite (adiabatic) surface
m	mean-mixing (bulk average) value
n,m	eigenvalue and summation indices

TABLE OF CONTENTS

Page

LIST OF FIGURES

LIST OF TABLES

1. INTRODUCTION

Interventional devices employing shape memory polymer (SMP) are increasingly being designed and tested for clinical use [1]. Unique properties of SMP allow for these devices to be crimped and fixed into a temporary shape for catheter insertion and then actuated at a site inside the body so that the SMP recovers its original configuration [2]. These "smart material" properties are useful in treatment of aneurysms [3,4], vascular stents [5], removal of blood clots [1], and an array of other surgical applications.

The external stimulus required for SMP actuation *in vivo* must heat the polymer above its predetermined glass transition temperature (T_g) to decrease the elastic modulus of the material and for shape recovery to take place [2]. Although some applications find it advantageous to use SMP with a T_g around body temperature (37°C) and depend on body heat alone for actuation, intravascular devices that must retain their crimped configuration inside a catheter during tortuous vessel navigation require a higher T_g in order to overcome absorption effects of T_g depression [6] and prevent premature actuation. Once at the deployment site, an external stimulus provides enough energy to actuate the higher T_g SMP. Various mechanisms can act as stimuli for shape recovery, but this study focuses on laser energy delivered through optical fiber to locally heat the SMP above its glass transition temperature. This non-physiologic energy entering the body calls for investigation into possible harmful effects on blood and vessel walls.

This thesis follows the style of *IEEE Transactions on Biomedical Engineering.*

Potential actuation sites inside the body are located in a variety of geometries, such as spherical aneurysms or cylindrical blood vessels. Before such complex scenarios can be theorized, the problem must first be greatly simplified in order to gain a critical understanding of the variations in fluid motion and thermal gradients for a catheter delivered device. To begin, assume two-dimensional steady, incompressible, fully-developed laminar flow in a long straight circular tube. The experimental fluid is Newtonian and has characteristic density and viscosity similar to blood [7]. Within the flow, a cylindrical metal cap models a generic SMP device secured to a hollow glass rod serving as a mock delivery catheter. Optical fiber running through the glass rod delivers infrared (810 nm) laser light into thermal epoxy within the metal cap resulting in localized heating representative of a generic SMP device actuating in the body. The effects of convective cooling are determined by varying flow rates inside the tube and energy delivered to the cap.

Equipped with two high-speed charge coupled device (CCD) cameras, an objective lens, and a very thin Nd:YAG light sheet, the experimental techniques of particle image velocimetry (PIV) and laser-induced fluorescence (LIF) can elucidate velocity fields and thermal gradients, respectively. Both techniques rely on seeding the fluid with the appropriate tracer particles and then imaging their interactions with the light sheet. For PIV, the cameras capture light reflected off of spherical glass particles suspended in the fluid and determine the distance traveled by each particle between successive frames. In contrast, ratiometric (or “two-wavelength”) LIF calls for two different optical filters that allow one camera to record the baseline temperature

independent Rhodamine 110 emissions while the other camera records the temperature dependent Rhodamine B fluorescence when excited by the 532 nm light sheet. Hence the name, the ratio between the two dyes, once calibrated, determines temperatures and their gradients across the field of view.

2. BACKGROUND AND SIGNIFICANCE

With researchers and clinicians working together to create innovative medical devices that are bio-friendly, more efficient, and easier to implement, the patient's safety remains a critical concern. Along these lines, testing the device and its impact on flow patterns, shear stresses, thermal shock, and weakened vessel walls helps evaluate its overall safety and viability when compared to critical values in the literature. Thermal damage to red blood cells is attributed to conformation changes in their membrane structural proteins, and the heat causes the normally biconcave erythrocytes to turn biconvex, then spherocyte. Partial membrane fragmentation results in loss of hemoglobin and the membrane disintegrates into globules before aggregating to form a mesh [8]. Based on the Arrhenius damage integral, the damage threshold for tissue necrosis occurs when the thermal damage coefficient equals unity [9].

2.1 Shape Memory Polymer Actuation

Properties of shape memory polymers have found application in numerous fields, including early ideas like automatic car chokes, over-temperature trip mechanisms, and shape adaptive compliant surfaces for robotic prehension [10]. Many studies have gone into detail on the phenomena underlying shape memory behavior in SMP. For the purposes of this study, only thermally activated SMP devices in medical applications are considered.

Actuation of SMP can be achieved through introduction of an external plasticizer or by thermal methods such as laser (photothermal) [11], [12] or electroresistive heating [13]. Additionally, successful actuation using Curie-thermoregulated inductive heating was reported, in which ferromagnetic particles were loaded into the SMP and exposed to an alternating magnetic field [14]. Methods of direct laser heating that use a diffusing fiber scattering light straight into the SMP and surrounding blood usually rely on a wavelength-specific dye to aid in absorption, such as Epolight™ 4121 [3], [11], [13] or indocyanine green (ICG) [12]. Since actuation occurs more rapidly nearer the fiber/SMP interface, an increasing dye concentration gradient stronger at the distal end has been suggested to reduce required laser power and result in a more uniform axial temperature distribution [12]. However, since the laser light in this study is converted to thermal energy within the epoxy before radiating through the metal cap, this experiment focuses on forced convection heat transfer, not the effects of light propagating through SMP devices into blood.

For laser heated SMP devices ($T_g > T_{body}$), the energy required for actuation holds the most potential for blood or tissue damage. Ideally, no more heat should be used than necessary to raise the SMP just over its glass transition temperature and for uniform shape recovery across the whole device. In practice, it has been established that internal flow rate affects localized heating and thus successful device deployment [3], [5], [11]. The heat carried away by convective cooling necessitates increased energy input to ensure full actuation because the flow generally carries the extra heat downstream of the device and concentrated towards the center axis (maximum velocity) of the tube. Note

that when the device is not concentric within the channel and angles towards the wall instead, CFD simulations show the heat being carried to a distal portion along the wall before trending towards the center axis, indicating a site for potential tissue damage [15].

2.2 Modeling SMP Behavior

Much attention has been given to actuation sites in aneurysm geometries, where SMP foams could fill the aneurysm, direct blood flow back through the parent vessel, and prevent rupture of the weakened aneurysm walls. A laser-activated foam device in an *in vitro* basilar aneurysm model shows successful treatment, with the flow rate (0-148 cc/min) affecting foam expansion and temperature at the aneurysm wall [3]. At zero flow, full expansion and overheating occurs at the aneurysm wall. Low (diastolic) flow reduces expansion time and increases temperature rise while high (systolic) flow results in incomplete expansion [3]. In a similar aneurysm geometry, CFD simulations of idealized spherical SMP foam predicts a 25°C worst case wall temperature rise at the aneurysm's apex, where the greatest isolation from convective cooling exists [4]. The same geometry was investigated with PIV, showing qualitative agreement with those previously mentioned [16]. In a separate research group's aneurysm model, comparison of PIV and CFD measurements for the same model provides validation [17].

Many applications of PIV have been published. Investigations of abdominal aortic aneurysms [18], saccular basilar aneurysms [16], and flow around stents [19] all demonstrate the effectiveness of PIV methods applied to intravascular issues. In cases

where CFD was simultaneously employed, overall agreement between the simulations and experiments is observed.

On the whole, applications of LIF are less represented in the literature, but some relevant articles do arise. The case of a heated cylinder in cross-flow is investigated with molecular tagging thermometry [20] and laser-induced fluorescence [21], with results showing qualitative agreement. Whole field temperature measurements using rhodamine dyes are performed by Sakakibara *et al.* [22] and Coolen *et al.* [23] in which the investigated temperature ranges were 40 K and 0.7 K, respectively. Two different CFD codes [24] for analyzing the case of a heated cylinder show qualitative agreement with experimental results from Hui [20] and Seuntiens [21].

2.3 Experimental and Theoretical Techniques

As seen in the literature review, a multitude of techniques can be employed to gain flow and heat transport information. This study implements a combination of PIV and LIF for experimental data and corresponding analytical and CFD results for theoretical comparison. Each technique's methods, specifics, and contribution to the study will now be assessed.

2.3.1 Particle Image Velocimetry (PIV)

Given a camera (or two cameras for stereoscopic PIV) focused on the flow channel with fluid moving left to right, x-scale, and the diameter of the channel is seen in the vertical direction, y-scale, a thin illuminating light sheet must be oriented

perpendicular to the cameras' field of view to collect PIV images (Figure 1). The light sheet is centered on the axis of the flow channel and focused down to a thickness of 100 µm with a sheet height of 23 mm. At this thickness, the diameter of the light sheet is more than 10 times smaller than the 6 mm tube diameter and provides adequate spatial resolution with minimal erroneous data. If the light sheet were too thick in comparison to the tube diameter, reflections from particles outside the center axis would be out of focus and skew the data, contradicting the assumption that only a single slice is imaged. The height of the light sheet runs parallel to the direction of flow and partially determines the maximum width of the field of view.

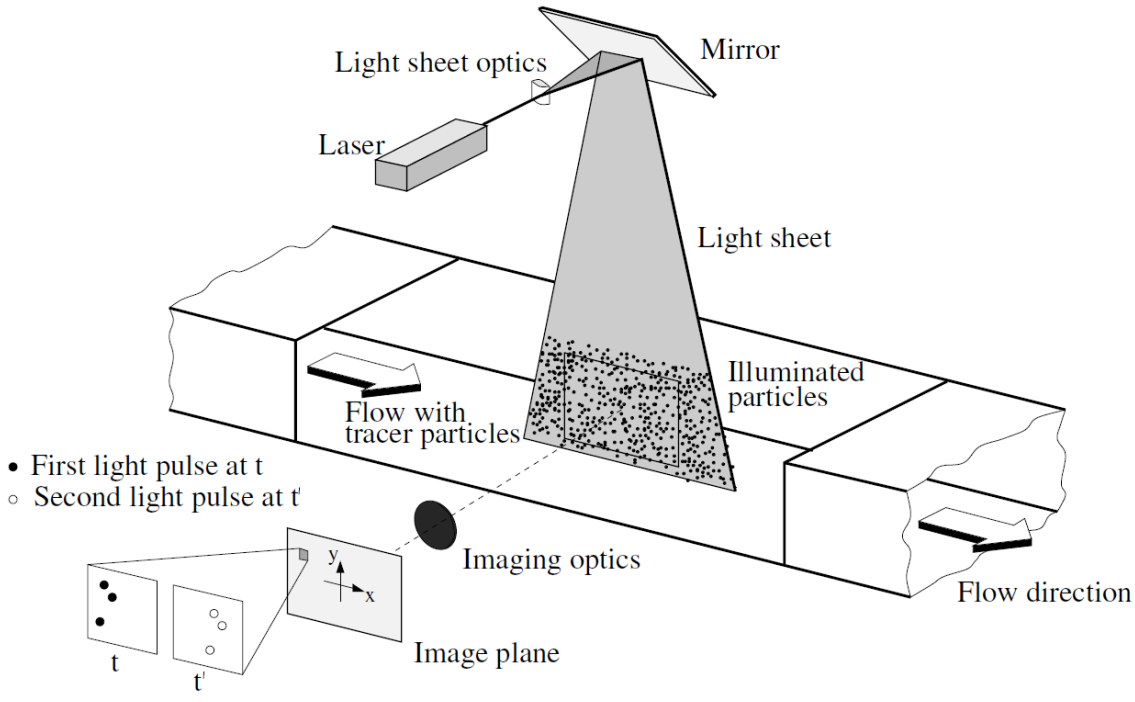

Figure 1 - Typical PIV configuration[1]

[1] With kind permission from Springer Science+Business Media: Particle Image Velocimetry - A Practical Guide, 2nd ed., Chapter 1, printed 2007, pg. 4, M. Raffel, C.E. Willert, S.T. Wereley, and J. Kompenhans, Figure 1.4, © 1998.

With the cameras and light sheet aligned and focused on the experimental model, the fluid is seeded with tracer particles that reflect the incident light sheet into CCD cameras to produce intensity mappings. Seeding particles used in this experiment, hollow glass spheres with average diameters of 9-13 μm, provide evenly distributed intensity patterns used for PIV vector calculation. The light reflected into the cameras at the same wavelength as the incident laser is due to Mie scattering, a solution of Maxwell's equations for spherical particles. Note at low Stokes and Reynolds numbers, the particles will adequately follow the flow [25], an important assumption inherent in all PIV applications. Previously, titanium dioxide played the role of seeding agent but it tended to clump together and cause large intensity spikes, attach to the device and dirty the channel walls, and generally did not dissolve well in solution or sufficiently follow the flow.

Now that all the physical elements are in place, how can light reflected from a particle in the fluid lead to velocity vectors? Consider only a single laser pulse exactly synchronized with a single recorded frame. The laser acts as a "flash" for the CCD camera to collect a frame of intensity information at one point in time made up of intensity spikes from each illuminated particle in the field of view. Analysis of a single image, however, can only determine instantaneous spatial position of each tracer particle, not local fluid velocity. To do so, the laser light sheet is double pulsed with a set time interval, dt, in between each pulse that is synched to two successive frames from each camera. Based on how far a particle shifts from the first frame to the next, the change in position is calculated first in pixels and then scaled to millimeters after camera

calibration. The time between the two frames (or pulses) is prescribed through DaVis software and enforced by a Programmable Timing Unit (PTU) linking the camera frames and the illuminating flashes. Together, the change in position, *dp*, and change in time, *dt*, determine velocity vectors, *v*, for each particle from one of the simplest derivative equations,

$$v = \frac{dp}{dt}. \tag{1}$$

For clarification, the lowercase *p* represents position and is not to be confused with the pressure gradient $\frac{dP}{dx}$, the change in pressure with respect to axial position.

Each image is divided up into small interrogation windows and the peak particle reflection intensities between the two frames are correlated with

$$C(dx, dy) = \sum_{x=0,y=0}^{x<n,y<n} I_1(x, y) I_2(x + dx, y + dy),\ -\frac{n}{2} < dx, dy < \frac{n}{2} \tag{2}$$

where *C(dx,dy)* is the correlation strength dependent on displacements *dx* and *dy*, and *n* is the size of the interrogation window in pixels.

After initial vector calculations, batch processing of the entire dataset deletes spurious vectors, smoothes out curves, interpolates over empty spaces, and averages over the whole set of 100 frame pairs (assuming steady flow) to remove any imaging artifacts. The resulting velocity map can then be used to determine velocity profiles, wall shear stresses, and a throng of other useful graphs.

A combination of adequate seeding density, well placed image masks, and small multi-pass interrogation windows provides sufficient spatial resolution in the critical regions near the walls to obtain a velocity profile consistent with the “no slip” boundary assumption, which states that fluid velocity at the wall is the same as velocity of the wall, or zero in this case. Raw data in the form of intensity mappings was collected with a known time displacement of 80 µs. From cross-correlation between successive frames, vectors were calculated and displayed with color-coded velocity scales (Figure 2).

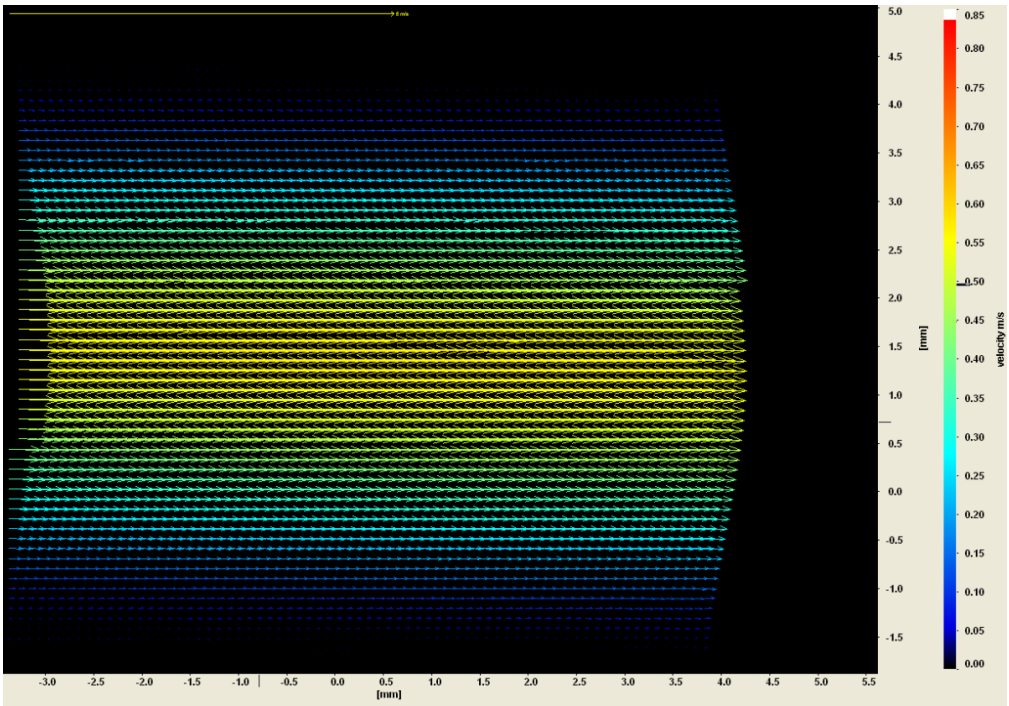

Figure 2 - PIV vector field for Poiseuille flow

A primary indication of the PIV system’s accuracy is obtaining the Poiseuille solution (Equation 4) for laminar, incompressible, pressure driven flow in a long

cylindrical pipe, exhibiting a parabolic velocity profile similar to expected flow patterns downstream of the device. Since flow is steady, the entire set of 100 image pairs were averaged together to smooth out the velocity vectors before extracting a velocity profile from successive points along a vertical line perpendicular to flow. Root mean square (RMS) deviation between analytical and PIV profiles (Figure 3) was determined as 1.55% and 2.25% for cases of low and high flow, respectively.

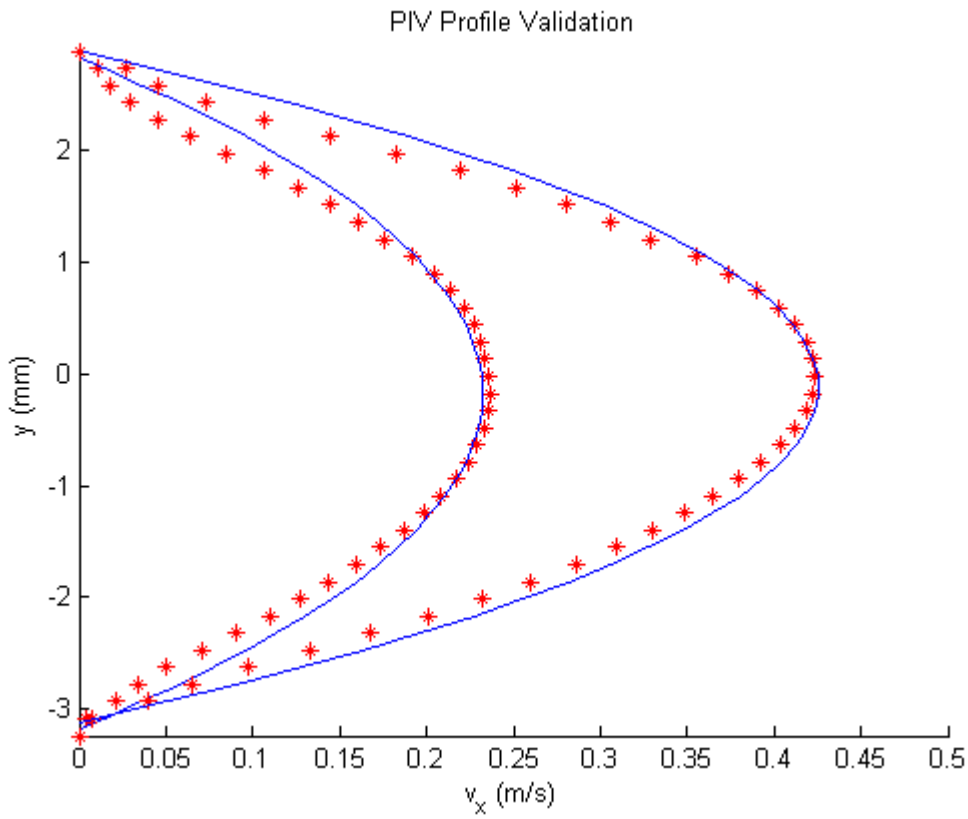

Figure 3 - Corresponding velocity profile for Poiseuille flow

PIV has its limitations, however. Most notably, the technique relies on passage of light which requires a transparent fluid, meaning that solid objects in the field of view

will block light passage and create a dark “shadow” where particles cannot reflect and thus vectors cannot be calculated. If the light sheet is oriented slightly behind the solid object, some light can get through and no shadow is observed, though this approach slightly changes the imaging plane and may skew the data. In the interest of accuracy, it is best to keep the light sheet in the center plane and impose an axisymmetric assumption such that the flow region shadowed by the cap corresponds to flow patterns on the opposite side where illumination is not a problem. Furthermore, the intensity of light reflecting off of a large metal surface is much greater than the intensity of reflections from the tiny seeding particles and can permanently over-saturate and damage the CCD chip. To alleviate this problem, any metal surface in the field of view is coated in bright neon fluorescent paint to dampen harmful reflections.

Prominent fluctuations in the flow field stem from fluid initially flowing in the annulus created by the catheter device inside the model, passing around the metal cap, and finally converging downstream to straight tube flow. The change in cap temperature, i.e., increased input laser power, does not affect the flow patterns significantly, except for small decreases in fluid viscosity and a resulting increase in local velocity. All flow rates considered here display laminar properties and an expected increase in velocity with increasing flow rates.

2.3.2 Laser-Induced Fluorescence (LIF)

Using the same basic setup as PIV, with the light sheet still perpendicular to the objective lens, the fluid is now seeded with two fluorescent dyes instead of spherical

glass particles and laser-induced fluorescence (LIF) can be used to visualize heat transfer. Interestingly enough, a similar form of LIF is used to measure concentration of solutions, but is employed in this project strictly for thermal measurements.

The two seeding dyes, Rhodamine 110 and Rhodamine B both absorb laser light at 532 nm, the wavelength of the Nd:YAG illumination source. In order to detect the difference in fluorescence from the two dyes, different filters must be used on each camera (Figure 4). A high pass (or long pass) filter on the first camera at 600 nm only captures the temperature-dependent Rhodamine B emissions, while a band pass filter on the second camera centered on 550 nm only detects the temperature-independent Rhodamine 110 emissions. Heat is then determined ratiometrically from the baseline emissions of Rhodamine 110 and the temperature dependent emissions of Rhodamine B. The same concept can be applied for 1-wavelength LIF, in which only one dye is used, but disadvantages include a dependency on concentration and a variation of intensity from light refracting through the thermal field. In contrast, the ratios determined by the 2-wavelength technique are nearly independent of incident light intensity and tracer concentration [22].

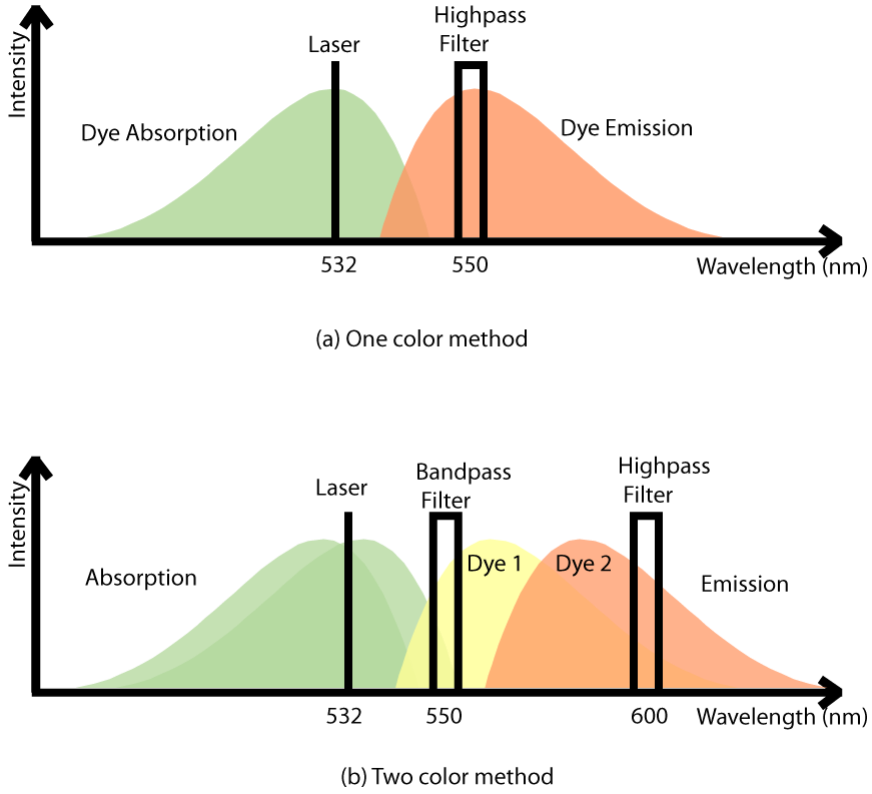

Figure 4 - Filter placement for LIF dyes (adapted from user manual)

After subtracting out the background emission intensity (or camera dark current) and correcting for inhomogeneities in the light sheet, the resultant temperature gradient qualitatively characterizes the change in heat around the device. To convert the heat ratios into usable temperature values, Rhodamine B emissions are correlated to the temperature range seen in the experiments. This was accomplished by heating the fluid with a hot plate near its point of entry so that the fluid in the field of view is isothermal. Calibration images were taken in about 5 degree increments from room temperature up to around 60°C. In each image, the emission ratios remain constant and can be

associated with each specific fluid temperature to obtain a quantifiable relationship (Figure 5). Note the intensity scale on the vertical axis refers to the ratio between dyes.

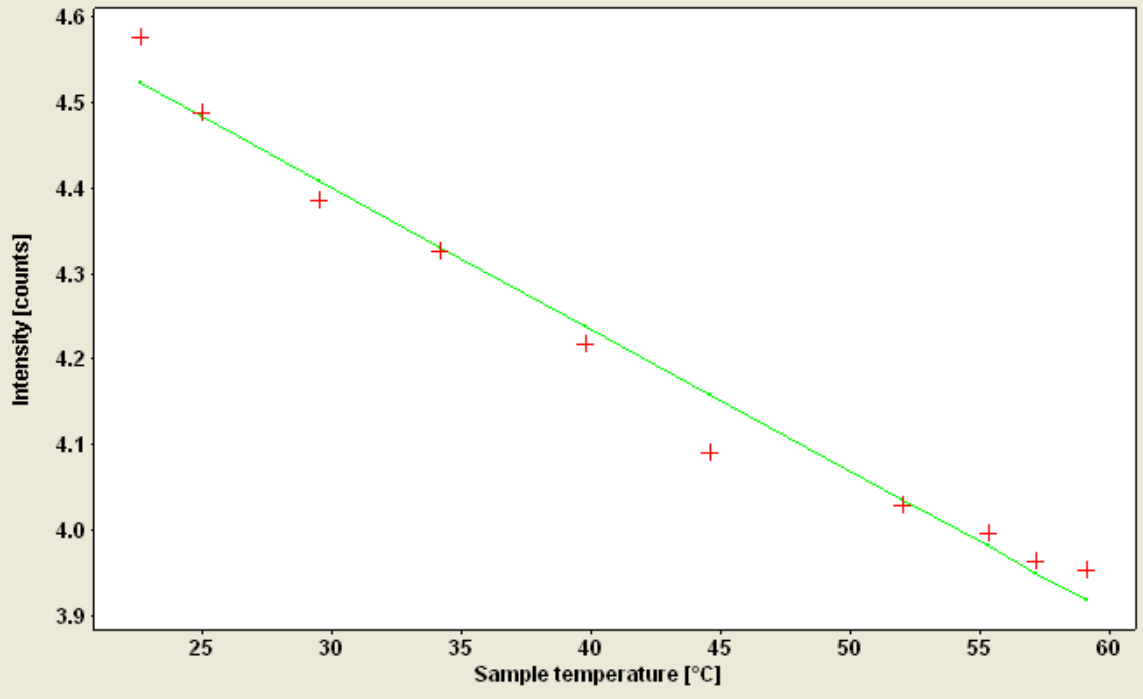

Figure 5 - LIF ratio temperature calibration

As is customary, post processing is needed to transform the raw images into useable metrics, except now the correlation is not between particle positions from frame to frame (as in PIV), but rather between the ratios of thermally dependent and independent fluorescence. In this sense, LIF processing is more of a pixel by pixel approach, and not nearly as robust as PIV, although the LIF processing does take much less computational time. Once again, the assumption of steady flow allows all images in a set to be averaged together, decreasing imaging artifacts and future processing time.

First, the raw images from each camera must be perfectly aligned, by determining disparity vectors from point correspondences or specifying a constant pixel shift, in order for pixels between the two images to correspond to the exact same point in the model. After recording the temperature calibration images, the necessary steps of background subtraction and sheet correction lead to a set of two images with only the pure fluorescent signal of either Rhodamine 110 or B in each. Then, the ratios of temperature dependent to non-temperature dependent emissions are calculated for each isothermal image in the two-color thermometry algorithm to associate each ratio for every given temperature (Figure 5). In general, the same processing steps for the isothermal calibration images is repeated for the experimental images, except using the calibration gained from the previous step to calculate spatial temperatures.

2.3.3 Techniques in Conjunction

Experimentally, PIV and LIF are very similar in that they use the same equipment oriented in a similar fashion. The only differences are in the choice of seeding particles, necessity of optical filters, and obviously the post processing algorithms, though the interrogation methods are similar.

Since PIV only obtains flow fields and LIF only finds temperature distributions, they are complementary modalities that can be simultaneously incorporated. With the current lab setup of two cameras and one illumination laser without an axial scanning mirror, the system is capable of running 2-D (single camera) or 3-D (two cameras, stereoscopic) PIV in a single data cycle. On a different run, the system can perform 1-

wavelength (one camera) or 2-wavelength (two cameras, ratiometric) LIF. Theoretically, the same system could execute 2-D PIV and 1-wavelength LIF simultaneously with a single camera reserved for each modality, collecting temperature and flow data at the same time. Although attempted several times, simultaneous PIV and LIF measurements were not attained for this particular application, probably due to the choices of laser wavelength, fluorescent dyes, and optical filters. Unfortunately, Mie scattering from particles in the fluid was observed through the bandpass filter, adding many small high intensity spots to what is supposed to be pure Rhodamine 110 emissions. Even averaged out across 100 images, the intensity spikes greatly affect ratio calculations. Regardless, the same information can be gained from two independent runs (PIV and LIF separately) at similar flow rates and overlaid to gain a more complete picture. Taking into account the significantly lower noise levels in 2-wavelength LIF, a superposition approach maximizes the accuracy and potential of each imaging modality individually yet limits the degree to which the two results (velocity vectors and temperature fields) can be directly compared. For instance, the model or device can never be guaranteed in the exact same position and the working fluid only lasts for a few days before switching it out. Much care was taken to ensure the controlled flow rates and heating inputs were identical across measurements, though some discrepancies are attributed to the omission of sodium iodide for the LIF fluid since it was showing up as noise in the Rhodamine 110 emission images.

2.3.4 Computational Fluid Dynamics (CFD)

Another method for modeling flow and heat transfer applications that are too complex for analytical methods, CFD, requires heavy computational power in order to iteratively solve the conservation equations across a discrete mesh. A representative model was drafted in a CAD program of the device within a 6 mm artery from which a volume mesh and subsequent velocity fields (Figure 6) were generated in Star-CCM+. Mesh cell sizes, especially in the boundary regions, are critical to computing acceptable results, and a grid independence test was performed by doubling the number of cells until observed changes in the resultant velocity profiles were less than 7%.

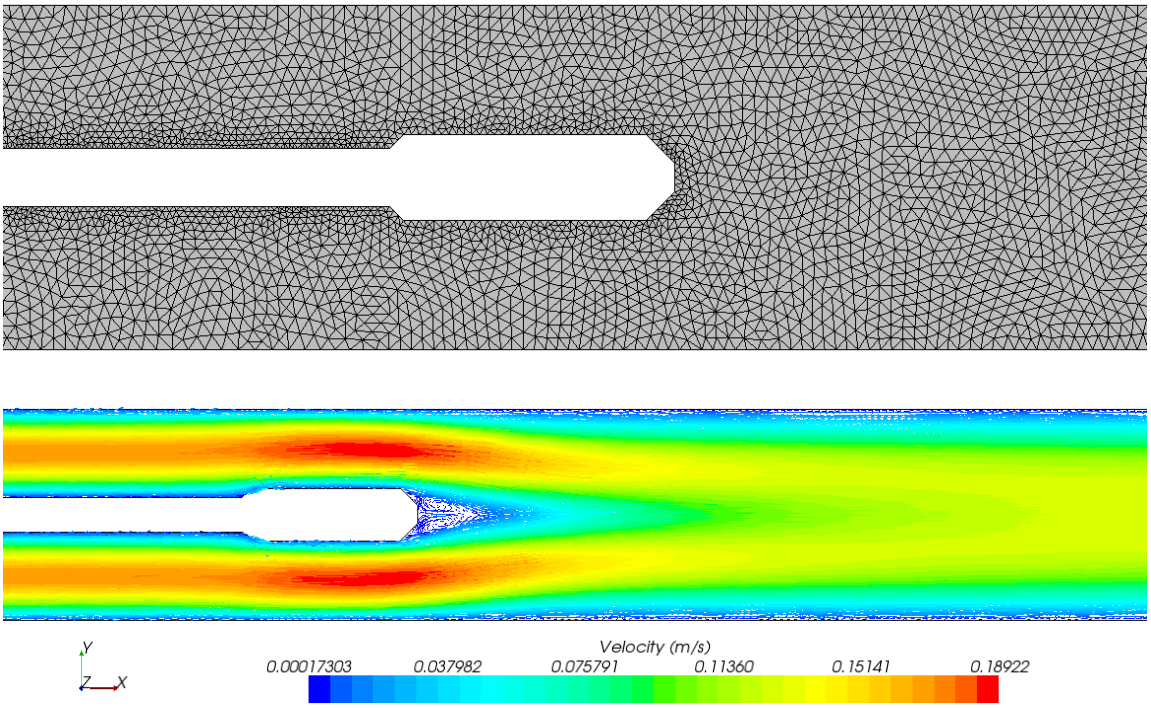

Figure 6 – Mesh geometry (top) and vector velocity field (bottom)

After specifying physical properties of the fluid (density, viscosity, and thermal conductivity), flow conditions, heat delivered inside the cap, and appropriate boundary conditions, the equations governing balance of mass, momentum, and energy were solved in an iterative fashion until minimal residual values (absolute error) were observed and thus reliable levels of convergence are met. Velocity profiles at distinct axial locations (Figure 7) before and after the metal cap were then extracted from the solved velocity field.

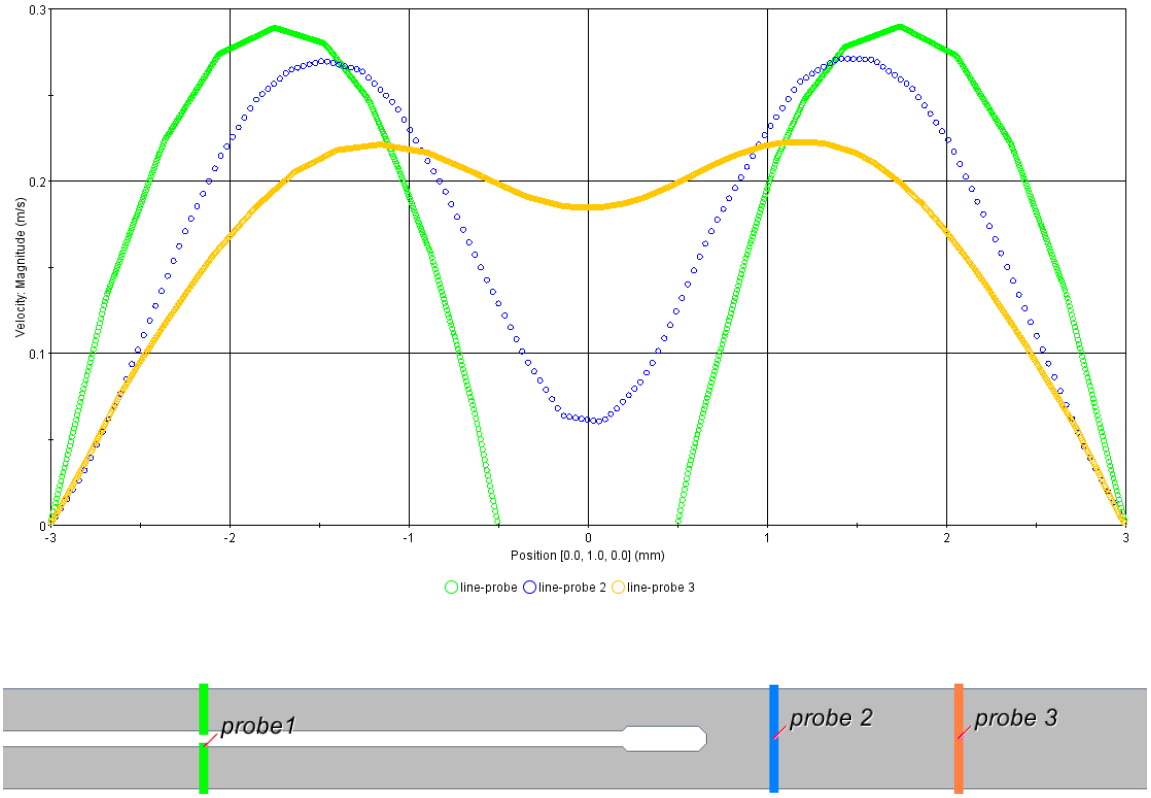

Figure 7 – CFD velocity profiles and corresponding axial locations (color coded)

CFD simulations have the freedom to easily change scope from micro-scale disturbances all the way up to atmospheric air flow, which allows investigation of entry effects, reattachment lengths, and heat flow past the device until it fully dissipates and body temperature is restored. Conversely, PIV is limited to a field of view (FOV) created by the objective lens and the height of the light sheet (measured in the direction of flow). At the laser's working focal length of 300 mm, which slightly compromises sheet height in favor of minimal sheet thickness, the sheet dimensions are 24 mm by about 100 μm. At most, 24 mm in the direction of flow are illuminated and can be imaged, limited by lack of intensity correlations in dark regions. The cameras also limit the FOV, each operating at full 1376x1040 pixel resolution with 1x magnification. In the best case, where the objective is focused so that the full diameter of the flow channel, 6 mm, is contained in the CCD chip's vertical direction, 1040 px, about 8 mm in the direction of flow can be imaged with a pixel resolution of 6.45 μm.

In this scenario, flow patterns near the point of entry (between concentric cylinders) and also far downstream of the device (Poiseuille pipe flow) are remarkably simple and the bulk of analysis resides in the region directly past the heating device. The extended entry region in the CFD simulations, similar to imaging near the distal end of the PIV experimental model, ensures fully developed entry flow. Although the limited experimental FOV does not extend far enough to document full convergence to straight pipe flow, CFD simulations indicate no major phenomena in this region.

3. MATERIALS AND METHODS

To incorporate the PIV/LIF system largely described earlier, a physical model and most of the complementary parts were designed and manufactured in house, and an integrated control and data acquisition system was coded in LabView. The acrylic mold for the idealized artery model was cut by the CNC [Roland MDX 540], most mounts and adapters for the flow loop were built on the 3D printer [Fortus 360mc], and the catheter heating device was hand assembled from metal caps milled to specification [MiniMachine] and hollow glass rods [Sutter Instrument Co.]. The thermally dissipative device serves as a disturbance to flow and also a source of local heat flux, the main concerns of this study. To investigate device effects under near-physiologic geometries and conditions, such as a cylindrical vessel full of blood-like fluid, the polydimethylsiloxane (PDMS) model artery was connected in a simple flow loop with a pumping mechanism and a recycling reservoir all connected with quarter inch tubing.

3.1 Experimental Setup

Experimentally, the setup includes controls for flow and energy input as well as imaging hardware (Figures 8 and 9). One computer controls the pump, heating laser, flow meter, and thermocouples, while a separate computer synchs the illumination laser with each frame grabbed by the CCD cameras and also handles the vector processing.

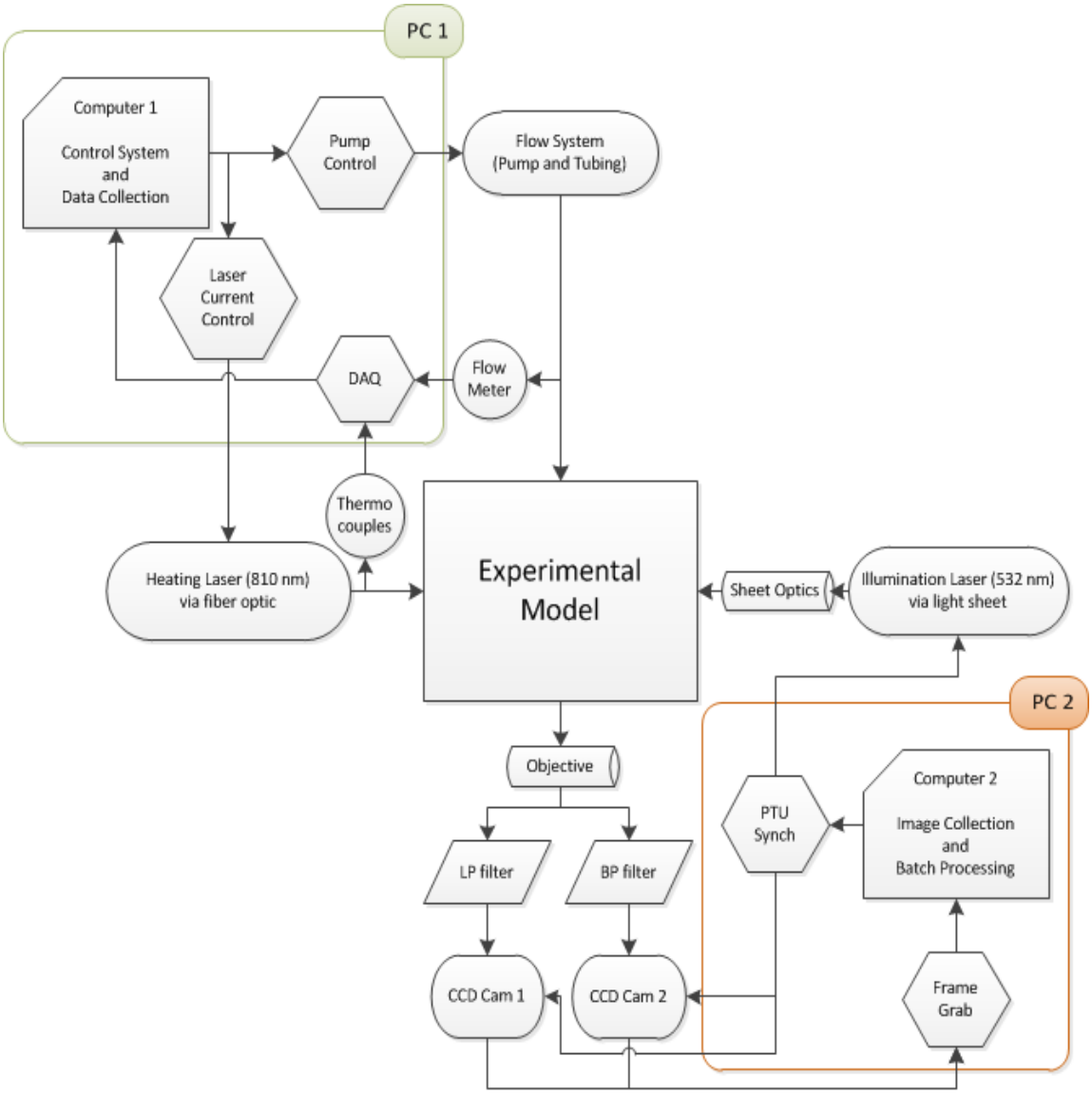

Figure 8 - Diagram of experimental setup

The bottom and right sides of the diagram are components of the PIV/LIF system, while the top and left sides are device heating and pump control, where each input combination is imaged by the PIV/LIF system to determine effects of flow and heating rate. All of the experimental factors are observed in the central model. Variables

such as flow rate and input power are adjusted and PIV/LIF is performed to obtain differing velocity fields and heat gradients for each combination. Many components alluded to in the abstract diagram (Figure 8) can be seen in the photograph taken during a LIF experiment (Figure 9). The only differences in the PIV setup from that shown here include a clear fluid (pink color due to LIF dyes) and a gear pump replacing the gravity-fed system of peristaltic pump and elevated funnel (directly above top center of image).

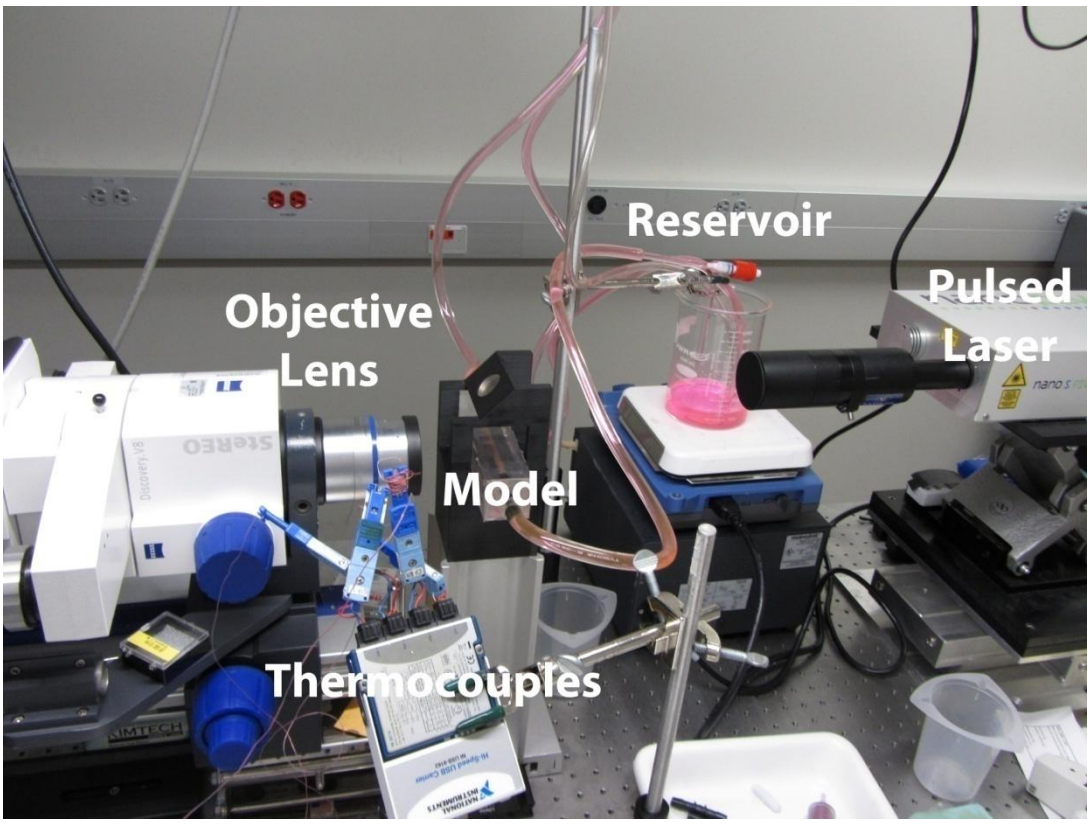

Figure 9 – Photograph of LIF experimental setup

The details of PIV and LIF have been summarized in previous sections; attention will now shift to model considerations including the heating device, working fluid within the model, and incorporated pumping systems.

3.2 Experimental Model

To represent an ideal noncompliant vessel with constant cross sectional area as a long straight tube, a rectangular acrylic mold was filled with freshly mixed components of PDMS [Sylgard 184, Dow Corning] in a 10:1 ratio and sealed at the edges with aluminum tape. Acrylic was chosen for its finished texture that yields a model with smooth surfaces on all sides and minimizes distortion in the cameras and light sheet. After tediously cycling vacuum inside a bell jar to remove all air bubbles in the liquid PDMS, the model was cured at 80°C for 1.5 - 2 hours. The mold yields a rectangular PDMS block of dimensions 3.82x3.82x20 cm and a steel rod spanning the full length creates the 6 mm diameter flow channel. The entire block is then secured directly in front of the cameras to a vertical support stand adjustable in the direction of flow, complete with a stationary mirror mount to direct the incoming light sheet past the top face of the model and through the center of the flow channel.

Fluid enters the model through a 3-D printed part combining a Tuohy-Borst adapter for device insertion, a nozzle for fluid entry, a method for attaching to the PDMS model (Figure 10), and a device alignment ring (not visible) near the model inlet. For PIV, a simple flow loop composed of a gear pump [R10616CB, Oberdorfer], quarter inch Tygon® tubing [Saint-Gobain], the above-mentioned Tuohy-Borst adapter, and the

PDMS model artery allows specification of flow rates based on gear pump revolutions per second. For LIF, the gear pump is replaced with a gravity fed system comprised of a peristaltic pump [Thermo Scientific] feeding an elevated funnel that minimizes particles in the flow.

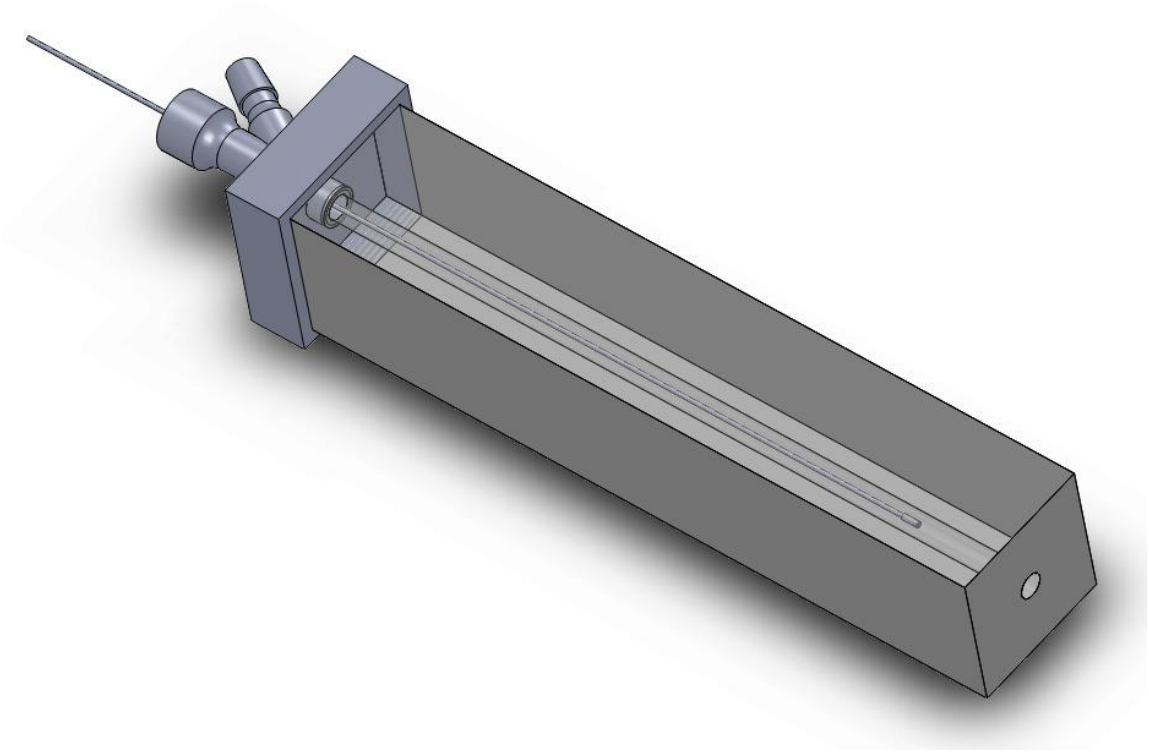

Figure 10 - PDMS model and device insertion

3.3 Device Design

Attention was first directed towards the design of the device in the context of modeling SMP heating. A cylindrical device shape is commonly observed in SMP medical devices, although they vary in shape and size depending on application. In their crimped state, vascular stents, spheroids for filling aneurysms, and some thrombectomy

devices assume a cylindrical form around a guide wire and/or a heating element inside a delivery catheter. The big difference between these listed medical devices and the experimental device (Figure 11) is that the latter has no shape memory effects and does not expand or change shape; it only increases heat dissipation with increasing laser power.

The thermal dissipation device represents an ideal case in which most of the laser energy delivered via optical fiber is converted into the heat necessary to push SMP above its T_g and back into its native configuration. A conductive epoxy injected into the core of the metal cap secures the optical delivery fiber as well as the accompanying thermocouple probes inside the metal cap. The epoxy also facilitates conversion of the 808 nm laser light into the thermal energy dissipating through the metal cap and to the surrounding convective flows.

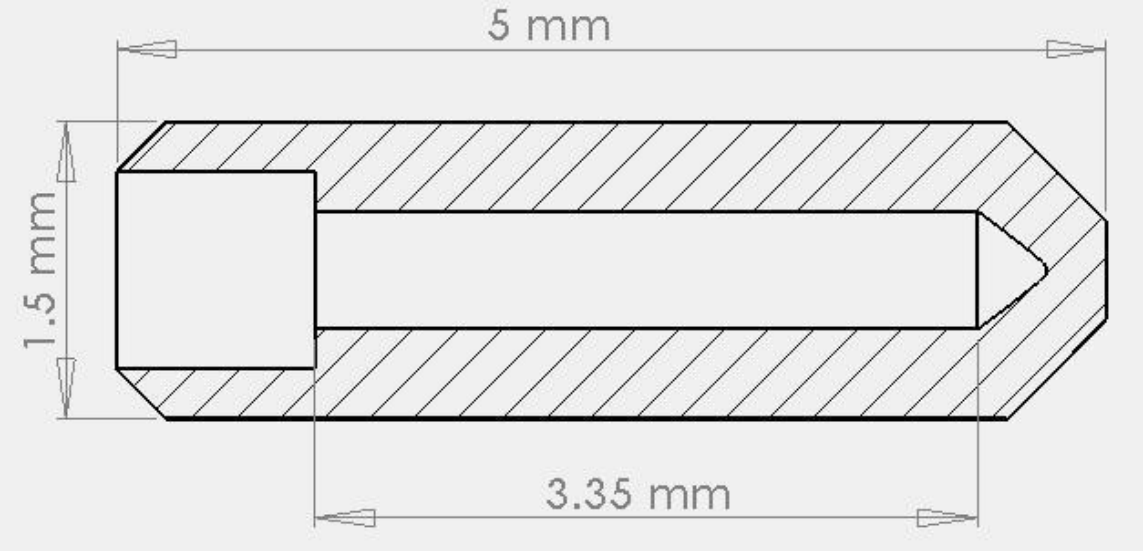

Figure 11 - Schematic of thermal dissipation device

Minimal components are assembled into the device (Figure 12): metal cap, glass rod, epoxy, thermocouple, and ST terminated optical fiber. Preliminary studies determined that stainless steel caps held up much better than aluminum ones that melted and lost their shape when subjected to heating. Kovar, a metal designed to match the thermal expansion coefficient of the glass rod, was also tested as a cap material. Hollow rods were cut to 25 cm lengths from borosilicate glass, with inner and outer diameters of 0.5 mm and 1 mm, respectively. The small volume of thermally conductive epoxy [H70E-2, Epo-Tek] inside the cap has a conductivity of 1 W/m/K to ensure efficient heat transfer throughout the cap.

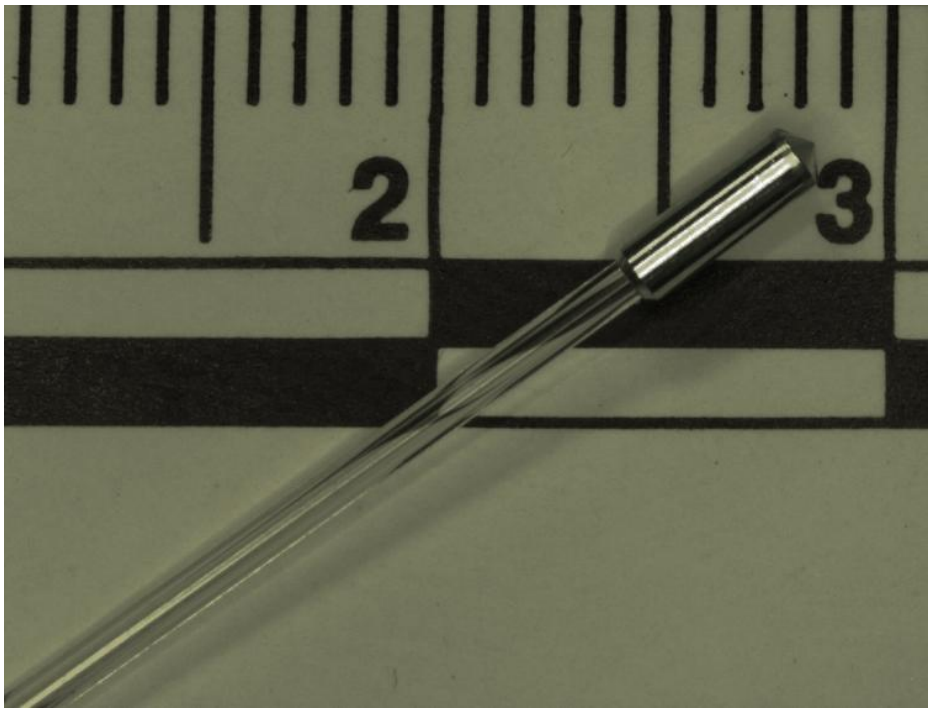

Figure 12 - Actual image of device attached to glass “catheter” (cm scale)

In order to measure the interior cap temperature, the junction of a bare 0.002" T-type thermocouple [Omega] is terminated in the epoxy just past the optical delivery fiber. Low OH (hydroxyl) fiber optic [Polymicro Technologies] was chosen with a core diameter of 200 μm and an attenuation of 7 db/km at 800 nm. Typically, low OH fibers are used for visible and near infrared (NIR) light while high OH fibers are primarily used for UV applications.

Given the appropriate components, device assembly begins with thermocouple and optical fiber preparation. One end of the fiber is terminated in an ST connector for hooking up to the heating laser and one lead of the bare thermocouple is sheathed in Teflon to prevent a short between the copper and constantan leads. Both are then threaded through the hollow glass rod until about 1.5 mm are protruding from the distal end before securing them in place with an airtight seal that also gives the flimsy glass rod some structural integrity. After calibrating the thermocouples, the glass rod is ready to be slid into the metal cap. First, thermally conductive epoxy is injected under vacuum through a modified 21 gauge needle with a flat tip that handily fits into the "catheter" slot of the cap to ensure that no air pockets form inside the cap which, when added with heating, would set it off like a rocket. When the inner cavity is completely filled, the excess epoxy is cleared out so that the glass rod has room to slide down the curing apparatus and nestle into the connection slot on the back of the cap (best seen in Figure 11) before curing at 115°C for a little over an hour.

3.4 Fluid Properties

The working fluid for PIV is composed of reverse osmosis water (47.38% by weight), glycerol (36.94%), and sodium iodide salt (15.68%). Mixed together in the appropriate weight ratio, they produce a transparent blood mimicking fluid (BMF) with key properties similar to blood (Table I) and a refractive index that matches the surrounding PDMS model [7]. A 60/40 mixture of glycerol and water is commonly used in biofluid experiments due to its physical similarity to blood (density and viscosity), and the sodium iodide was added to also match the refractive index of the PDMS model. It was found that sodium iodide did not work well with LIF imaging, where Mie scattering interfered with the Rhodamine 110 temperature independent emissions, so the working fluid for LIF is assumed to be the 60/40 glycerol and water mixture.

Table I Properties of Pertinent Fluids (note *by volume **by mass)

Property (at 20 °C)	Blood [11]	Blood Mimicking Fluid (BMF) [7]	Water
μ, Dynamic viscosity $\left[\frac{g}{cm \cdot s}\right]$	0.035	0.0431	1.002
ρ, Density $\left[\frac{g}{cm^3}\right]$	1.06	1.22	0.998
ν, Kinematic viscosity $\left[\frac{cm^2}{s}\right]$	0.033	0.035	1.004
k, *Thermal Conductivity $\left[\frac{W}{m \cdot K}\right]$	0.5195	0.492	0.58
C_p **Specific Heat $\left[\frac{J}{g \cdot K}\right]$	2.668	3.850	4.184

Images of various fluid compositions in the model were taken above grid paper to qualify differences in refractive index (Figure 13) and confirm the matching between blood mimicking fluid and the PDMS model. Notice the distortion of grid lines at the channel boundary in every image but the bottom right. For reference, refractive index

values are given as 1.0 for air, 1.33 for water, 1.4129 for the 60/40 mixture, and 1.414 for blood mimicking fluid and the PDMS model.

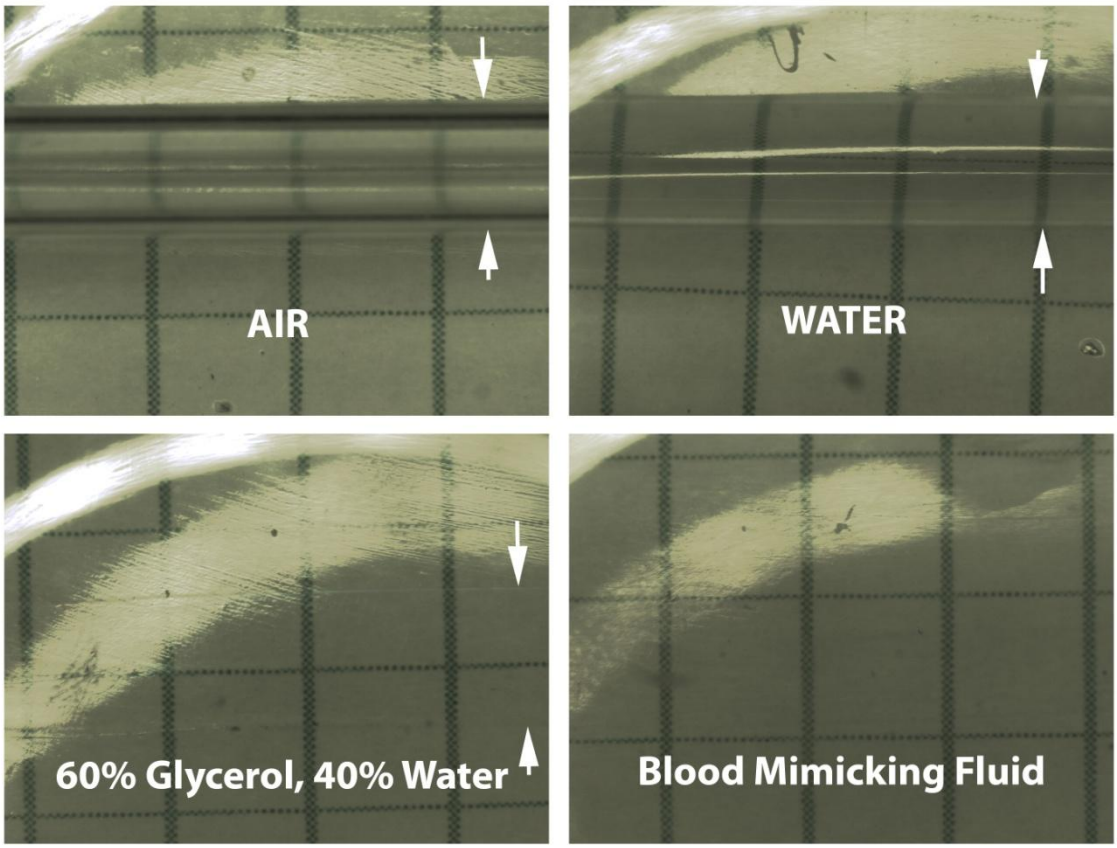

Figure 13 - Refractive index matching of fluid (arrows indicate flow channel diameter)

The speed of the gear pump [revs/sec] is calibrated to the flow rate [mL/min] by a linear relationship (Figure 14) obtained with a stopwatch and graduated cylinder. Calibration of the gravity-fed system (Figure 15), relates stopwatch measurements at constant height difference to concurrent digital flow meter [Omega FLR1000] readings, and a flow control valve at the outlet maintains the physiologically relevant flow rates.

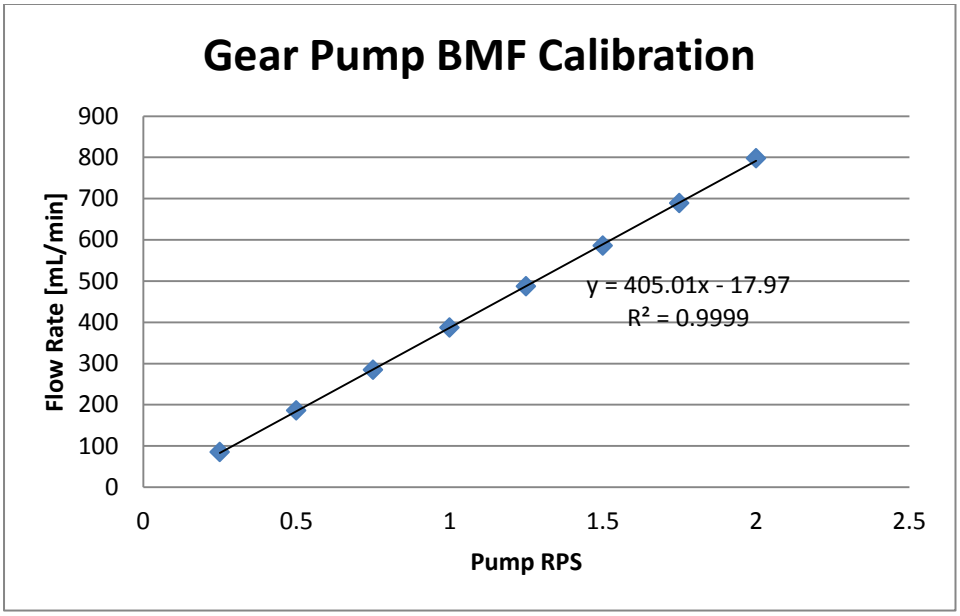

Figure 14 - Gear pump BMF calibration

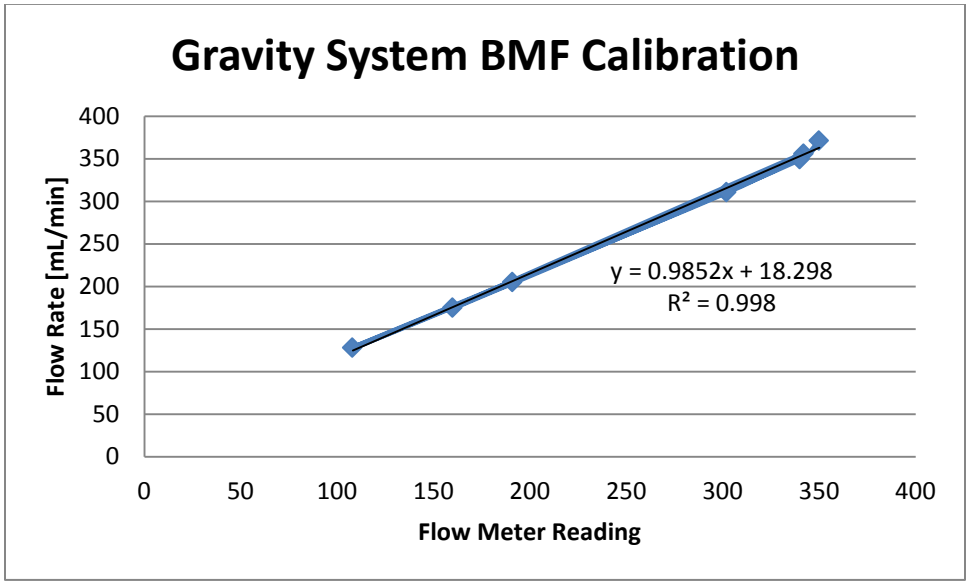

Figure 15 – Gravity fed system BMF calibration

In practice, both pumping systems provided steady flow at the required flow rates, though the gear pump system was much easier to control with its short commands and quick response time. Since the PIV images were recorded first, before discovering the gear pump's endless capacity of irritating particles, the gravity fed flow system for the LIF recordings attempts to match the previously considered flow rates, though the fluid composition slightly changed by omitting the sodium iodide and including isopropyl alcohol to initially dissolve the Rhodamine dyes before mixing it into a batch of experimental fluid. Physiologically relevant flow rates were determined by Reynolds number calculations (*see Section 4.1*) in order for results in the model to be applicable to *in vivo* geometries for a better understanding of how laser-activated interventional devices might affect the body.

4. ANALYTICAL APPROACH

Consider the current scenario in the most ideal conditions as a convection heat transfer problem with fully developed flow originating between concentric cylinders, i.e., annulus flow, and transitioning into Poiseuille pipe flow downstream of the heat source. Both simple pipe flow at the pressure outlet and concentric annulus flow at the entrance around the catheter heating device can be investigated independently by breaking the analysis into separate phases. To predict how the flow transitions from one phase to the next, computational fluid dynamics (CFD) iteratively solves the balance equations (*see Section 2.3.4*), essentially blending together the simple solutions shown in (Figure 16). The predictions from mathematical models provide a source of comparison for the experimental results of PIV and LIF. Several studies have found good agreement between CFD and PIV/LIF results [16], [17], [24].

Basic mathematical assumptions are enforced to obtain hydrodynamic solutions [29], [30], [32]; namely, incompressible fully developed laminar flow with constant (non-temperature dependent) and Newtonian fluid properties, velocity as a function of radius only, and viscous dissipation neglected.

The following segment is divided into sections for Reynolds number calculations, velocity profiles, temperature solutions, and further discussion. Logically, the physiologic body process is modeled experimentally and scaled by a characteristic dimensionless parameter from which flow patterns are theoretically known in two spatial

dimensions that determines the internal convective heat transfer for the geometries before, around, and past the heated portion of the catheter device.

4.1 Flow Similarity

When modeling a process within the body, the principles of similitude dictate that the model and real application share geometric, kinematic, and dynamic similarity such that the test results are applicable to the real design. With dynamic scaling and the aid of dimensionless parameters, various flow conditions in vessels of different sizes can all be examined in the same experimental setup. The choice of a cylindrical pipe model easily satisfies geometric similarity to a blood vessel. Further similarity is enforced through matching the Reynolds number,

$$Re = \frac{u_m D_h}{\upsilon} = \frac{QD}{\upsilon A}, \qquad \text{where } u_m = \frac{Q}{A}. \tag{3}$$

Using the fluid properties values in Table I and *in vivo* measurements of vessel diameters [26] and flow rates [27], the Reynolds number is first calculated for blood occupying a human artery. To test the device in a range of physiologic flows, consider the geometric relations of both the basilar and carotid arteries. For the basilar artery, flow rate is taken to be 100 mL/min with a vessel diameter of 0.323 cm, yielding a Reynolds number of ~200. In the carotid artery, flow rate increases to 350 mL/min and the diameter increases to 0.616 cm, with a resultant Reynolds number of ~365. The same relation (Equation 3) is then rearranged, maintaining the calculated Reynolds numbers

for both arteries, to solve for corresponding flow rate in the model using BMF properties (Table I) and the fixed model diameter of 6 mm. Results are summarized in Table II.

Table II Flow Similarity

	Q_{phys} [mL/min]	D_{phys} [cm]	Re	D_{model} [cm]	Q_{model} [mL/min]	Gear Pump [rev/s]
Basilar	100	0.323	200	0.6	197	0.53
Carotid	350	0.616	365	0.6	361	0.93

4.2 Velocity Profiles

Flow patterns in the field of view are limited to the two cases of annular flow around the catheter device converging to Poiseuille's solution for steady pipe flow downstream. In either case, derivation of the Navier-Stokes equations for the given assumptions and boundary conditions yields exact solutions for the velocity profile, *u*, and other quantities of interest such as flow rate and friction factor. For the simplest case, the parabolic velocity distribution due to pressure driven flow, or Poiseuille pipe flow, and the corresponding flow rate are given as

$$u = -\frac{1}{4\mu}\frac{\partial P}{\partial x}(r_o^2 - r^2) = u_{max}\left(1 - \frac{r^2}{r_o^2}\right) = 2u_m\left(1 - \frac{r^2}{r_o^2}\right) \quad (4)$$

$$Q = -\frac{\pi {r_o}^4}{8\mu}\frac{\partial P}{\partial x} \quad (5)$$

Solving (5) for the axial pressure gradient in terms of flow rate and directly substituting into (4), velocity profiles can then be plotted for both the low and high flow rates considered (Figure 16, low and high pipe flow). These analytical solutions provide baseline comparisons to evaluate the performance of the PIV system. Correlations between theoretical solutions and profiles obtained experimentally can predict the validity of results for when more complicated scenarios are investigated.

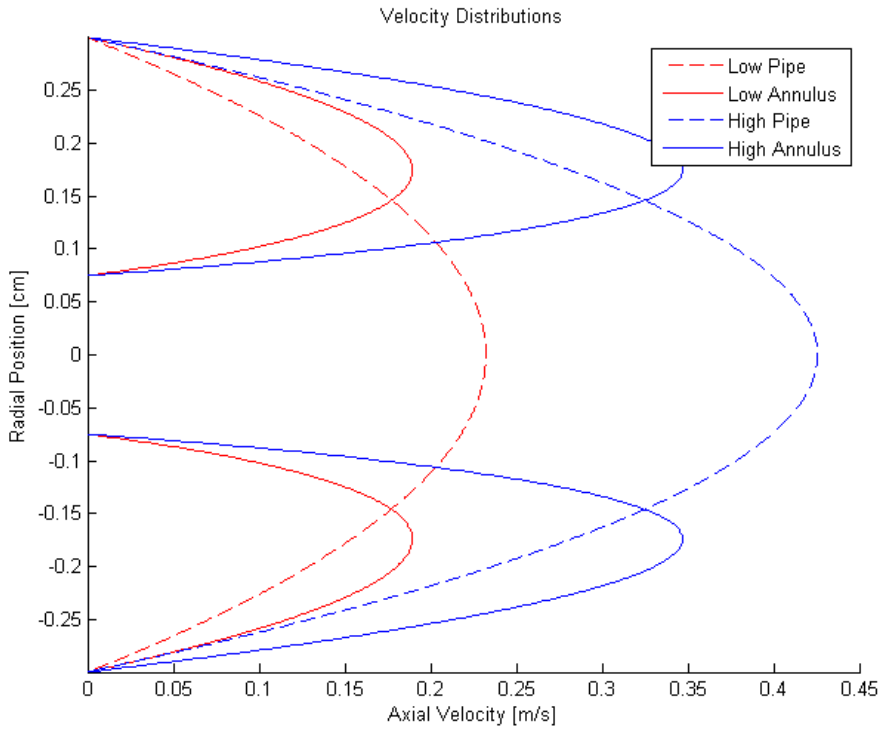

Figure 16 - Velocity profiles for pipe and annulus flow at two flow rates

Sources for annulus heat transfer in the literature most often cite Lamb [28] for the velocity profile in an annulus (Figure 16, low and high annulus flow), though its representation varies depending on the method of solution. For consistency throughout,

the equations cited are given in terms of the inner and outer radii, r_i and r_o, radius ratio, $r^* = r_i/r_o$, and normalized radius, $\bar{r} = r/r_o$. The corresponding annulus geometry is given in (Figure 17).

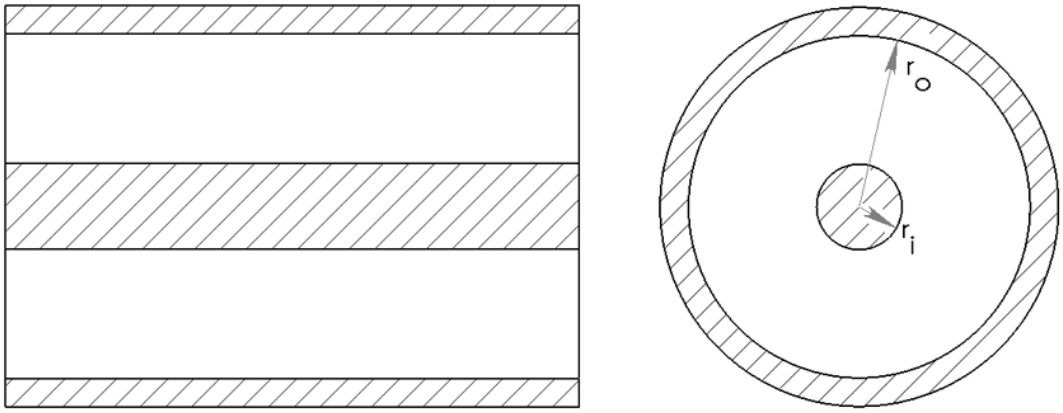

Figure 17 - Annulus coordinate system (front section, left; top section, right)

Here, the pertinent solutions obtained in the literature are only summarized. Further details of their methods and formulation are included in Appendix B. The equations for velocity distribution are given by Shah and London [29] as

$$u = -\frac{1}{4\mu}\left(\frac{dP}{dx}\right) r_o^2 \left[1 - \left(\frac{r}{r_o}\right)^2 + 2r_m^{*\,2} \ln\left(\frac{r}{r_o}\right)\right] \tag{6}$$

$$u_m = -\frac{1}{8\mu}\left(\frac{dP}{dx}\right) r_o^2 \left(1 + r^{*2} - 2r_m^{*\,2}\right) \tag{7}$$

$$\frac{u_{max}}{u_m} = \frac{2\left(1 - r_m^{*\,2} + 2r_m^{*\,2} \ln r_m^*\right)}{1 + r^{*2} - 2r_m^{*\,2}} \tag{8}$$

where r_m is the radius where maximum velocity achieves $[\partial u/\partial r = 0]$, and its dimensionless form, $r_m{}^*$, defined as

$$r_m{}^* = \frac{r_m}{r_o} = \sqrt{\frac{1-r^{*2}}{2\ln\frac{1}{r^*}}} \tag{9}$$

Transforming (6) and (7) into a notation consistent with previous literature (*see Nomenclature*) and noting that $\left[r_m^{*\,2} = B/2\right]$ and $\left[1 + r^{*2} - 2r_m^{*\,2} = M\right]$, the resulting equations are found to be identical to those reported by Lundberg *et al*. [30], [31] for velocity as a function of normalized radius,

$$u(\bar{r}) = \frac{2u_m}{M}(1 - \bar{r}^2 + B\ln\bar{r}) \tag{10}$$

and Worsoe-Schmidt [32] for normalized velocity, $\bar{u} = u/u_m$

$$\bar{u} = \frac{2}{M}(1 - \bar{r}^2 + B\ln\bar{r}) \tag{11}$$

Both Jakob and Rees [33] and Hatton and Quarmby [34] give the velocity distribution normalized by the inner radius rather than the outer (*see Appendix B*), but the latter equation does not include a variable radius (likely a misprint). Worsoe-Schmidt appears to be the only one to extend the original velocity distribution (Equation 11) to a series expansion for $-1 < R\bar{y} < 1$ in powers of $\bar{y}$,

$$\bar{u} = \frac{2r^{*2}}{M}[B\ln(1 + R\bar{y}) - 2R\bar{y} - R^2\bar{y}^2] = A\bar{y}(1 + \textstyle\sum_{n=1}^{\infty} a_n\bar{y}^n) \tag{12}$$

Using the dimensionless parameters, $R = s\frac{1-r^*}{\bar{r}_j}$, $\bar{x} = \frac{4x/D_h}{Pe}$, and $\bar{y} = s\frac{\bar{r}-\bar{r}_j}{1-r^*}$,

where $A = \frac{2R}{M}\left(B - 2\bar{r}_j^2\right)$, $a_1 = -\frac{R\left(B+2\bar{r}_j^2\right)}{2\left(B-2\bar{r}_j^2\right)}$, *and* $a_n = \frac{(-R)^n B}{(n+1)(B-2\bar{r}_j^2)}$, $for\ n = 2,3,\ldots$

It is interesting now to point out the two limiting cases of an annulus: the circular tube with an infinitesimally thin center wire ($r^*=0$) and the flat duct ($r^*=1$), both of which

can be represented by (12) with different coefficients than listed above and have equivalent solutions in the literature available for direct comparison.

4.3 Heat Transfer

After obtaining a velocity distribution for fully developed laminar flow in an annulus, the heat convection equations can then be solved for corresponding temperature profiles and put in terms of Nusselt numbers. A comprehensive study at Stanford University culminating in a series of papers on annulus heat transfer [30], [31] outline general problem formulation, solutions for hydrodynamically developed laminar flow, and solutions to more complicated scenarios that are not pertinent here. They consider four possible fundamental boundary conditions for annular geometries, depending on boundary conditions of temperature or heat flux specified at the walls. For each kind, there are two solutions to the energy equation, one for each of the heated surfaces, totaling eight heat transfer solutions. This study only considers fundamental solutions of the second kind, corresponding to a step change in heat flux at one wall while the opposite wall is maintained adiabatic (insulated), and further limits investigation to heating at the inner wall only. Therefore, the clarifying superscript (k=2) for solutions of the second kind is omitted for brevity.

Jakob and Rees [33] analytically obtain the temperature distribution for the basic case of both hydrodynamically and thermally fully developed flow. Hatton and Quarmby [34] find thermal entry solutions (hydrodynamically fully developed, thermally

developing) for the case of inner wall heating. Chien [35] considers the case where only a section of the inner cylinder is heated.

Lundberg *et al.* [30, 31] independently solve the thermal entry problem for all four kinds of fundamental solutions, based on the method of separation of variables and eigenfunction expansion for large values of x^* and employing the Leveque method near the point of step change for small values of x^*. Worsoe-Schmidt [32] bridges the gap between the limit for the Leveque solution and the point where the eigenvalue solution becomes manageable by considering a perturbation of the Leveque solution. Shah and London [29] present a summary of annulus heat transfer, including the works of all those recently mentioned, and blend together the solutions of Lundberg *et al.* and Worsoe-Schmidt for the thermally developing case.

4.3.1 Hydrodynamically and Thermally Fully Developed

Enforcing the assumption of uniform heating, $\frac{\partial T}{\partial x} = C = const$ and $\frac{\partial^2 T}{\partial x^2} = 0$, neglecting axial conduction, and defining temperature rise in the fluid for uniform heating from inside and perfectly insulating outside, $\theta = T - T_1$, Shah and London [29], citing Lundberg *et al.* [30] [31], give the dimensionless temperature and Nusselt number for the hydrodynamically and thermally fully developed case as,

$$[\theta_{oi} - \theta_{mi}] = r^*[\theta_{io} - \theta_{mo}] \tag{13}$$

$$Nu_{ii} = \frac{1}{\theta_{ii} - \theta_{mi}} \tag{14}$$

$$Nu_{io} = Nu_{oi} = 0 \tag{15}$$

where at the specified experimental radius ratio, r^*=0.25, the tabulated results give $[\theta_{io} - \theta_{mo}] = -0.102207$, $[\theta_{oi} - \theta_{mi}] = -0.025552$, and $Nu_{ii} = 7.75347$.

4.3.2 Hydrodynamically Fully Developed and Thermally Developing

For thermally developing solutions [30], [31], [32], Worsoe-Schmidt extends the Leveque-type (small x*) solution by obtaining the first seven terms (N=6) of the series (16) and reduces it to (17).

$$Nu_{x,ii} = \frac{1}{\frac{1}{2}\sum_{n=0}^{N}\left(\frac{36x^*}{A}\right)^{\frac{n+1}{3}}\theta_{j,n}(0) - [4r_i^*/(1+r^*)]x^*} \tag{16}$$

$$Nu_{x,ii} = 0.517(4A)^{1/3}(x^*)^{-1/3} = 0.517(f_i Re)^{1/3}(x^*)^{-1/3} \tag{17}$$

where $A = \frac{1-r^*}{r_i^*}\left[\frac{\partial(u/u_m)}{\partial(r/r_i)}\right]_i = \frac{f_i Re}{4}$ after some simplification.

Lundberg *et al.* give the results for large x* in a table, noting the bulk mean profile as a function of r* and x* and the dimensionless heat fluxes on the inner and outer walls,

$$\theta_{x,mi} = \left(\frac{4r^*}{1+r^*}\right)x^*,\ \Phi_{x,ii} = 1,\ \ and\ \Phi_{x,oi} = 0 \tag{18}$$

$$\theta_{i,fd} = \frac{r^*}{1+r^*}\frac{1}{M^2(1-r^*)^2}\left[\frac{1-B}{2}(\bar{r}^2 - \ln\bar{r}) - \frac{\bar{r}^4}{8} + \frac{B}{2}\bar{r}^2\ln\bar{r} - \frac{r^{*2}M}{2} + \frac{1+\ln r^*}{2} - \frac{r^{*4}}{8}\right] + \theta_{ii} \tag{19}$$

Note θ_{ii} is still undetermined and can be found by subtracting the bulk mean temperature profile, however, the equation given by Lundberg *et al.* is claimed to be in error by Shah and London. It is corrected in the temperature profile shown in (Figure 18) that combines the eigenvalue solution of Lundberg *et al.* for $x^* \geq 10^{-2}$ and the Leveque solution of Worsoe-Schmidt for $x^* \leq 10^{-2}$, where the values for θ and Nu at r^*=0.25 are given for a range of x*. Both curves (Figure 18) correspond to heating at the inner wall only, but the temperature profiles are evaluated at either the inner or outer wall (*see Appendix A*).

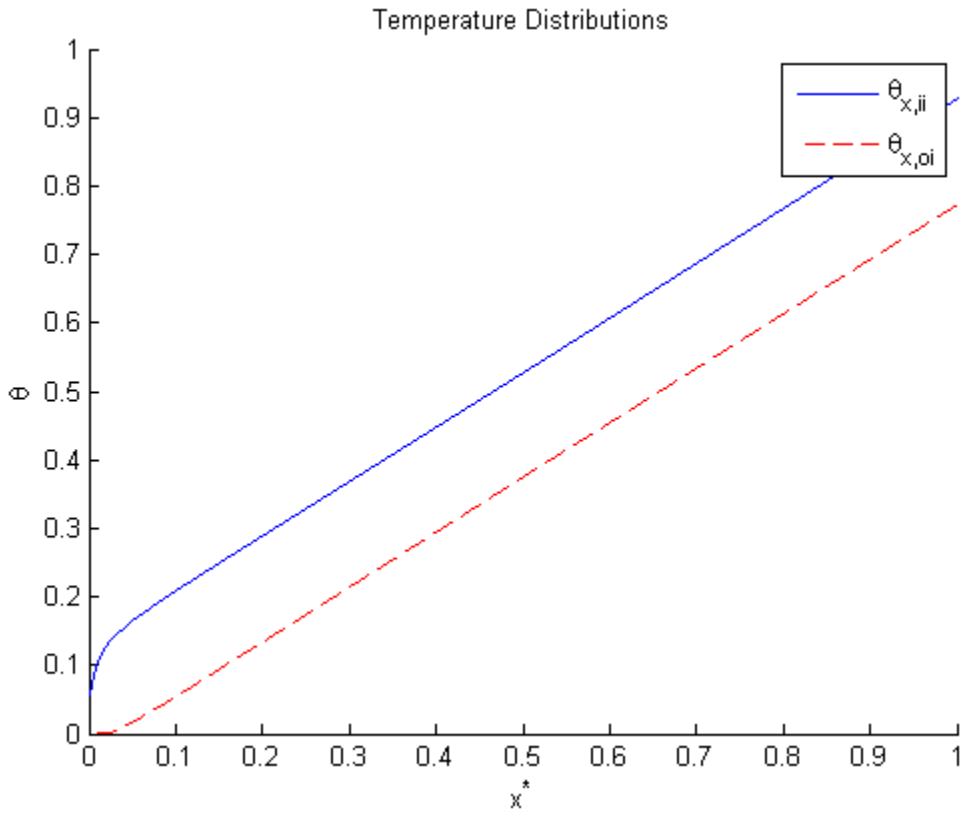

Figure 18 - Annulus temperature distributions

From the temperature profiles, Nusselt numbers at the inner and outer wall as a function of axial position are also calculated and presented by Shah and London (Figure 19). Hatton and Quarmby present eigenvalues and related constants in tabular form and $Nu_{x,ii}$ as a function of 4x* for r*=1/6, 1/3, ½, 1/1.5, and 20/21 that are in excellent agreement with those presented here. The same hydrodynamically and thermally developed equation for Nusselt number (14) is still valid for the thermally developing case shown here, only now the three terms also depend on x*.

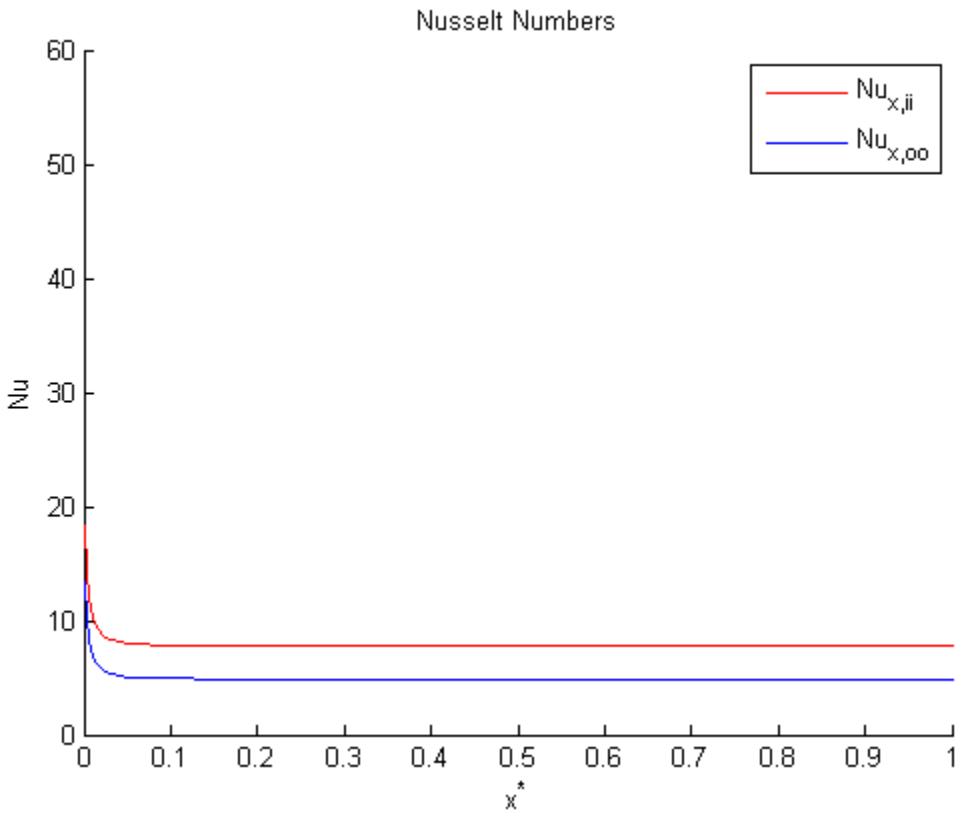

Figure 19 - Annulus Nusselt numbers

4.4 Additional Parameters

The Reynolds number (3), already given, depicts the ratio of inertial to viscous forces. For laminar flow in a pipe of diameter D, the laminar regime is observed if $Re_D \leq 2300$ and the entry length, x_{fd}, required for fully developed flow,

$$\frac{x_{fd}}{D} = 0.05 \cdot Re_D \tag{20}$$

For the given Reynolds numbers of 200 and 365, entry lengths are calculated as 6 cm and 11 cm, respectively, both of which are much shorter than the ~16 cm developing length allowed in all experiments.

The Prandtl number is very useful in heat transfer problems, a fluid property describing the interplay between viscous and thermal effects. Prandtl number or the working fluid, $\left[Pr = \frac{\nu}{\alpha} = \frac{\mu C_p}{k}\right]$ is calculated as 33.6, which lies in the range of blood (Pr=15-50) found in the literature. The Peclet number is introduced to consider the effect of fluid axial conduction. It has been found that the axial conduction of a fluid can be ignored when Pe > 10.

$$Pe = Re \cdot Pr = \frac{Rate\ of\ energy\ transport\ by\ convection}{Rate\ of\ energy\ transport\ by\ conduction} \tag{21}$$

At both high and low flow rates considered here, the Peclet number is much greater than the critical value of 10 and the assumption of neglecting axial conduction in favor of pure convection is found to be valid.

Additional relevant parameters include the Brinkman number, accounting for the influence of viscous dissipation [36], and the Grashof number, which approximates the ratio of buoyancy to viscous forces, or the relative importance of natural convection.

5. RESULTS AND DISCUSSION

The framework established in previous sections, including theoretical solutions for velocity and temperature fields as well as experimental system validation with simple scenarios, provides the means to investigate phenomena imposed by intravascular heating with a multi-pronged approach of PIV, LIF, CFD, and analytical solutions. When these assorted modalities agree on the same conclusions, the models are believed to be validated by the experimental results. By controlling like conditions throughout this study, the contribution from the most important variables of input energy and flow rate can be assessed.

5.1 Energy Input and Cap Heating

Using a 7.8 W diode laser [UM7800, Unique-m.o.d.e.] operating at 808 nm coupled to the epoxy within the cap through a 200 μm core diameter optical fiber, delivered input power is controlled through variable laser current. Laser power measurements were made before attachment to the device to correlate these two parameters (Figure 20).

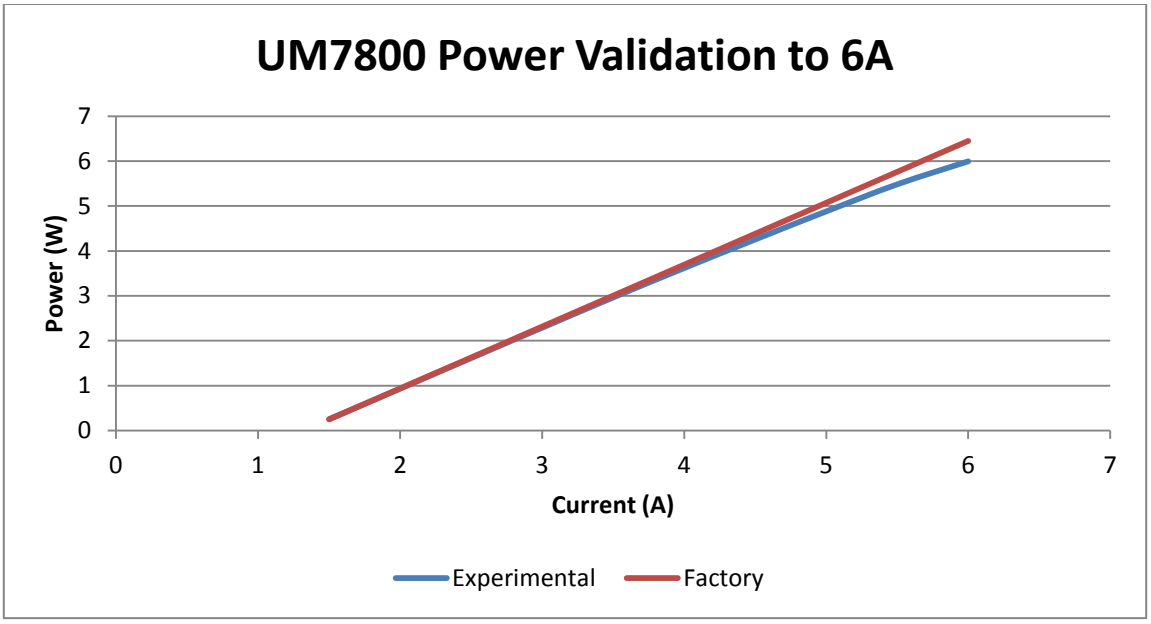

Figure 20 - Laser power measurements

The linear relationship above represents the amount of energy directed from the laser into the cap, but does not take into account energy loss in the fiber to fiber connection or reflections from the metal cap. To accurately determine the efficiency of the dissipation device itself, i.e., correlate laser current input to heat output, calorimetry experiments were attempted.

All temperature readings were accomplished with thermocouples which are then recorded via Labview into a text file for further analysis. Temperature measurements are important for several aspects of the project. The temperature of the epoxy inside the cap is directly prescribed in the CFD simulations as a starting point. While obtaining isothermal images for LIF calibration, temperature fluctuations inside the model were

determined to be less than 1 degree for each set of 100 images. Just as the images are averaged together, so are the temperatures observed during each recording.

For the considered high and low flow rates, as well as a very low rate for comparison, maximum temperature in the cap strongly correlates with lower flow rates (Figure 21). Although there were minor fluctuations in temperature readings when plotted against time, only the lowest flow rate (just a drip), produced very large sinusoidal fluctuations, most likely caused by natural convection.

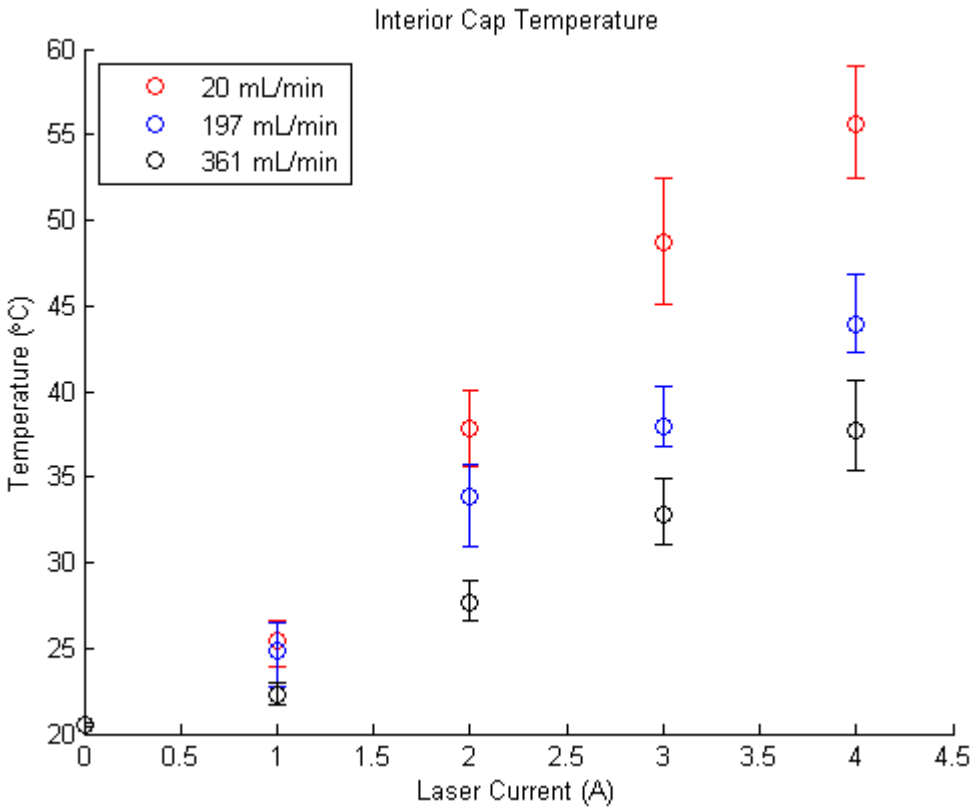

Figure 21 – Cap temperature during device heating (standard deviation error bars, n=3)

Although the cap was found to output roughly 90% of the energy from the laser, only when the heat is not carried away by convective cooling can maximum device efficiency be realized. Inserting the device into a sealed vial of water held between two large Styrofoam blocks [Texas Foam] with a small cut out channel for the thermocouple and fiber delivered optics, calorimetry experiments were attempted with limited success. For each incremental power input, the steady state temperature of the water was recorded. Along with the values in (Figure 20), the temperature measurements are used to calculate the efficiency of the device and determine the relationship between fluid temperature rise and the lasers only controllable input parameter: variable current. Both steady state and time resolved temperature measurements are required in very small increments for integration of the heat equation,

$$q = mC_p\Delta T, \tag{22}$$

where q is energy dissipated into the calorimeter, m is mass of water, C_p is specific heat capacity of water, and ΔT is the temperature rise.

5.2 Flow Fields

Fluid velocity fields were recorded for high and low flow for varying laser input current (0, 1, 2, 3 Amps). Scales for velocity components are color coded to the right of the image. Each combination was processed with the same mask (since the cap doesn't move), highlighting the effect of heating on flow fields. For example, the case of 3A heating at 197 mL/min (Figure 22) represents typical velocity vectors seen for every combination. The metal cap is the dark spot in the middle left and fluid flows from left

to right. Determining the effect increased heat has on the flow cannot be easily deduced from inspecting each vector field since they appear almost identical. Instead, velocity profiles from each image at the same distance past the cap were plotted (Figure 23). As expected, the profiles for both the low and high flow cases were close knit amongst themselves with the dip in the middle due to flow recirculation past the cap.

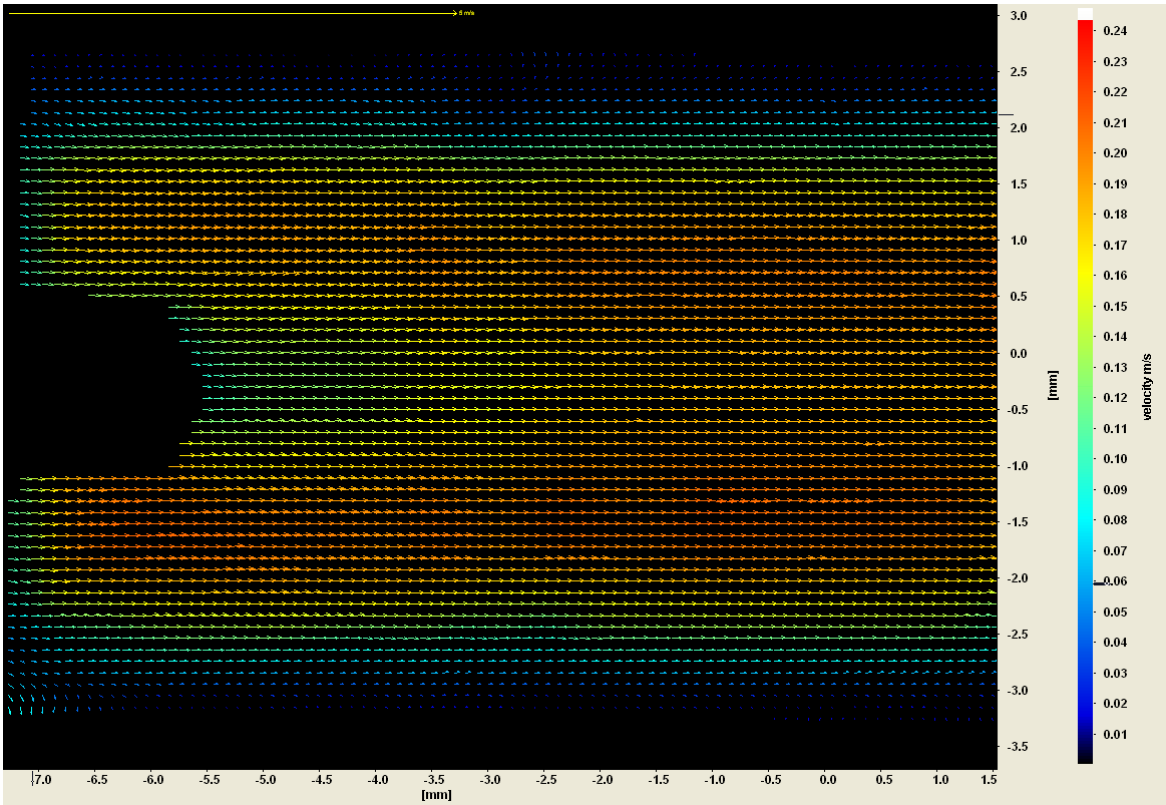

Figure 22 - Vector velocity field around device

When zoomed in on the center of the low flow profile (Figure 24), it is easily apparent that higher laser power results in higher local velocity. The same is true at the high flow rates. These results are in agreement with numerical analysis accounting for

temperature-dependent viscosity [47] showing that the lower viscosities present in the boundary layer tend to increase the local velocity values there.

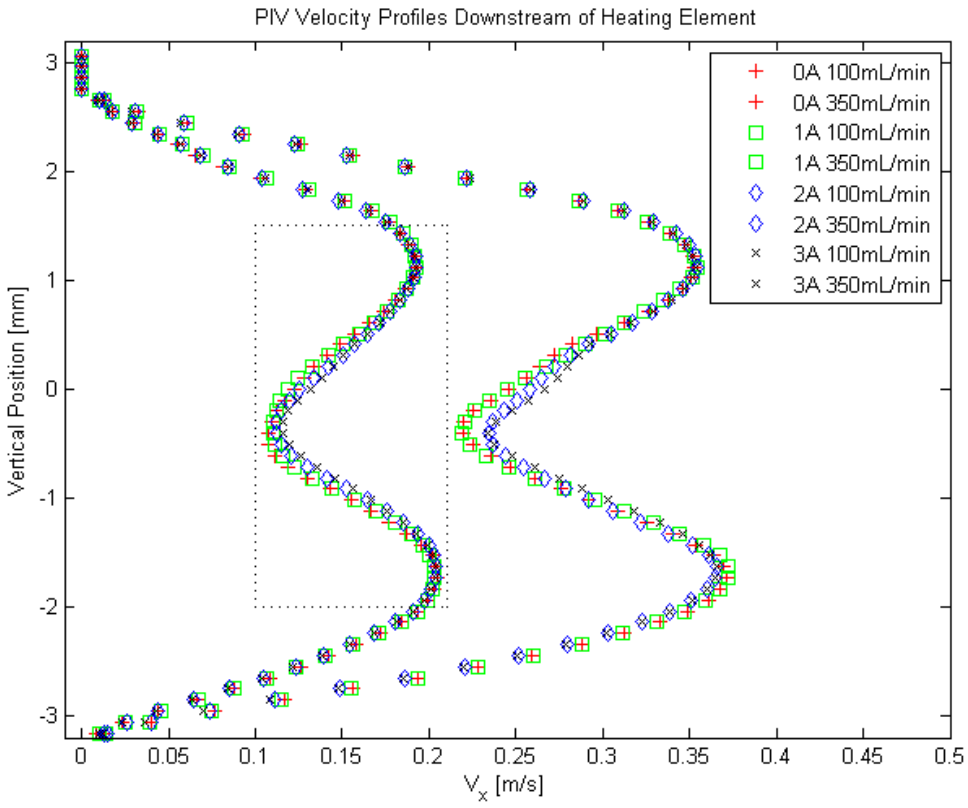

Figure 23 - Velocity profiles with varying heat for two flow rates

Comparisons shown in (Figures 23 and 24) illustrate the small effect of temperature on the velocity vectors. The four curves at different heating rates in the low flow case exhibited an average difference of 0.0029 m/s with a range of 0.0086 m/s. For the high flow case, an average difference of 0.0054 m/s and a range of 0.0153 m/s was observed. Although the analytical equations assume fluid viscosity independent of temperature for easier calculation, in reality viscosity tends to decrease with increasing temperature, such as honey or syrup pouring easier when heated.

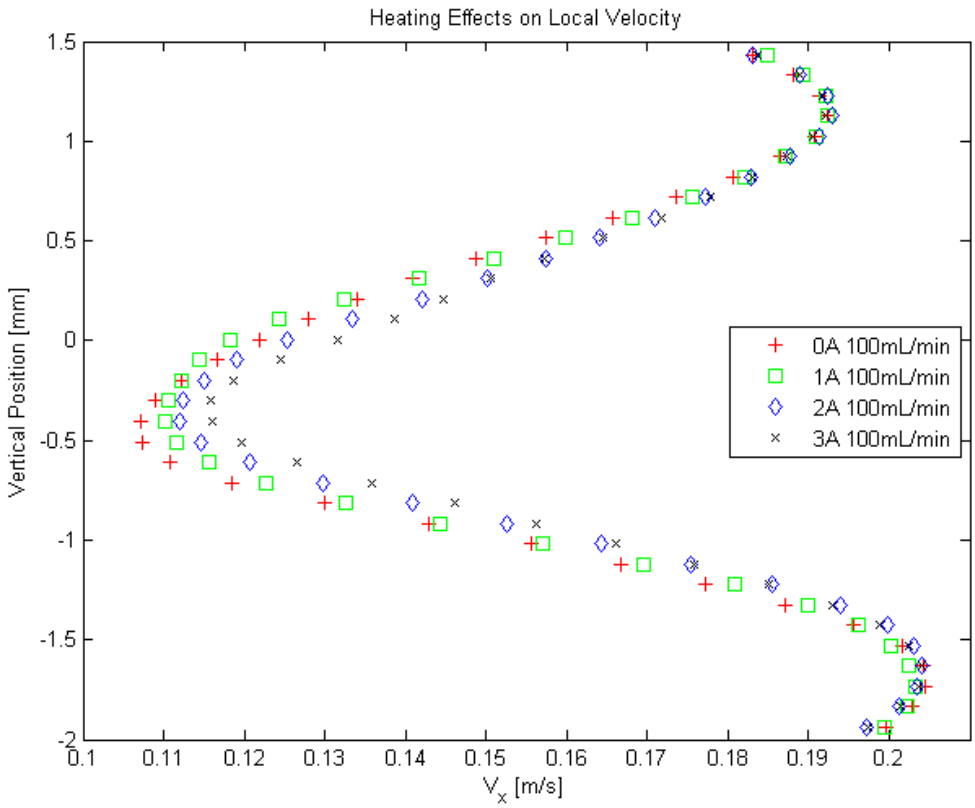

Figure 24 - Zoom of previous image to show heating effects

The variations in velocity were observed only in the region very near the cap, and flow near the channel walls was not affected, indicating that a vascular heating element even at low flow rates would jeopardize minimal blood cells, as long as convective cooling is allowed to do its part.

Similar to the validation case of straight Poiseuille pipe flow (Figure 3), velocity distributions are compared between CFD modeling and PIV experimentation for annular flow (Figure 25) with an error of 0.0587 and 0.1092 for the low and high flow cases, respectively.

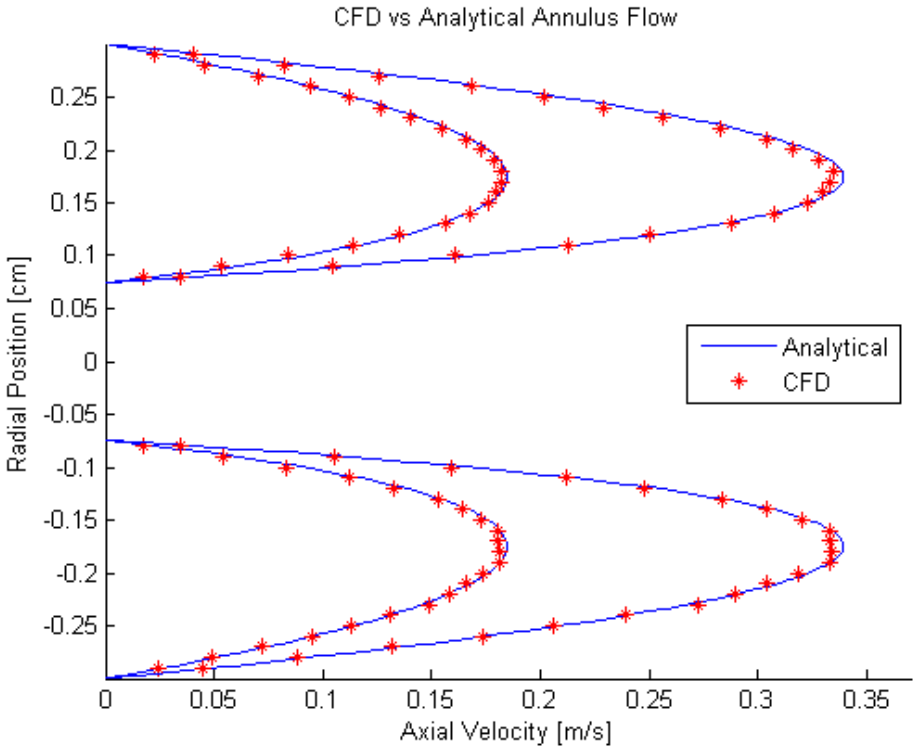

Figure 25 – Comparisons between analytical and CFD annulus profiles

On the whole, disruption of flow due to a centered device was minimal and distal reattachment lengths were quite short, with maximum velocity shifting from the point described by (Equation 9) in annulus flow to the center axis of the tube past the device. When the cap is angled towards the wall, it creates a region of higher shear stress near the wall and skews maximum velocity components towards the slant direction of the device [15], possibly inflicting damage on vessel walls where convective currents are weakest.

To obtain velocity profiles (Figures 23 and 24) with spatial resolution high enough to depict no slip boundary conditions at the walls and elucidate the minute

differences imposed by different heating rates, adequate seeding particles and small interrogation windows (leading to more smaller vectors) were crucial. Also, the mask that crops out both the device and the tube walls followed each interface very carefully in order to reduce artifacts at the boundaries. When time averaging image sets together, any movement of the device from frame to frame can cause misalignment of the mask and result in spurious vectors at the fluid-cap interface.

PIV results in this section reveal fluid activity in the transition not only from annular to pipe flow, but also from heated to unheated regions, which requires more complicated analytical equations and CFD simulations can only primitively predict.

5.3 Temperature Fields

Temperature fields were recorded for the same cases of low and high flow (197 and 361 mL/min) and laser currents (0, 1, 2, 3, 4 Amps). Maximum temperature rise inside the device depends on which cap material was used. Stainless steel caps led to much higher temperatures than those made from kovar. A cap temperature of 150°C was prescribed for the simulations in Figures 26 and 27.

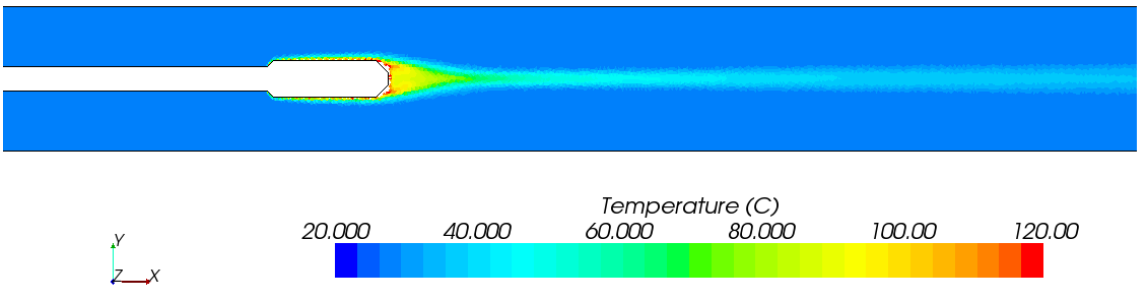

Figure 26 - Temperature field for low flow

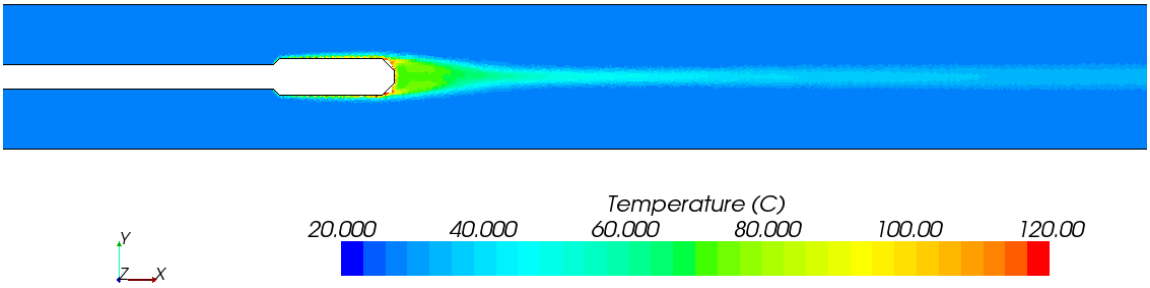

Figure 27 - Temperature field for high flow

As input power was increased, cap temperature and surrounding fluid temperature also increased. The hottest portions remain just distal to the cap and the majority of heat was carried down the center axis of the tube with the maximum velocity of the convective current. To quantify the differences imposed by varying flow rate, temperatures were extracted along a line probe (Figures 28 and 29) in the center of the tube from the tip of the cap all the way to the far right side of the temperature fields.

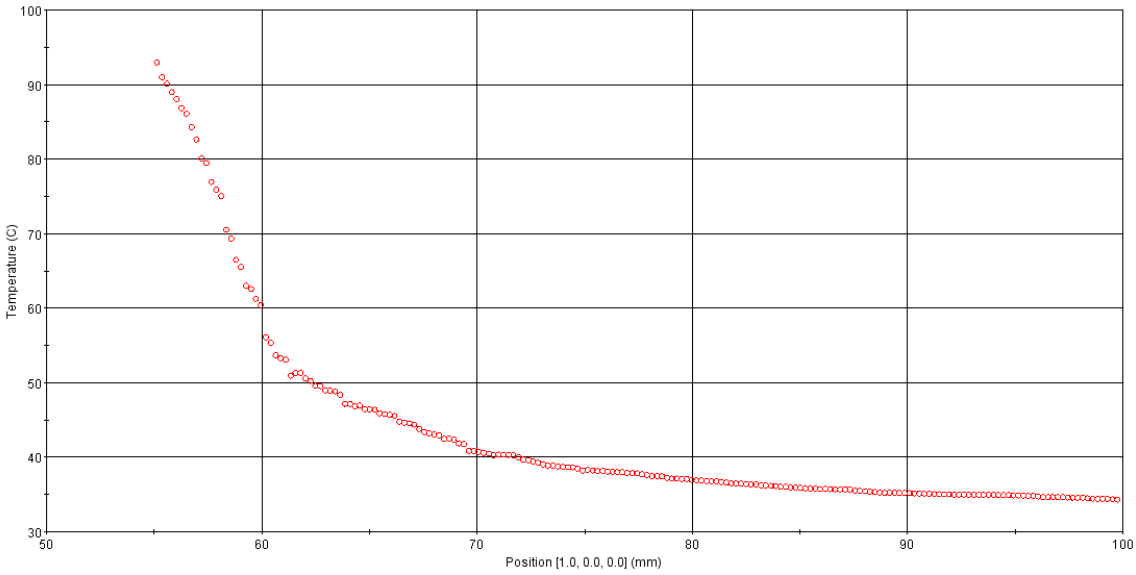

Figure 28 – Centerline temperatures for low flow distal to cap

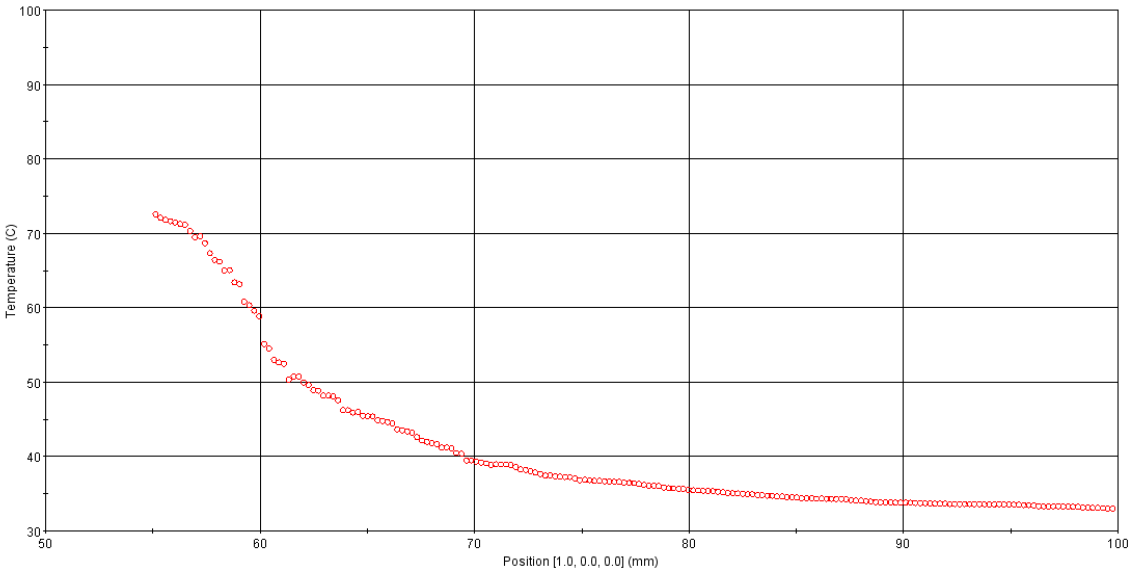

Figure 29 – Centerline temperatures for high flow distal to cap

Maximum temperatures beyond the cap were recorded as 93°C for the low flow case and 73°C for the high flow case before both trending towards room temperature. As shown, the higher velocities carried the fluid away from the heat source more quickly, giving the fluid less time to absorb heat from the metal cap. About 2.5 cm distal to the cap, there is not much discernible difference between the two flow cases, suggesting that the influence of the heating element is minimized and heat is dissipated to the colder fluid closer to the channel walls.

6. SUMMARY AND CONCLUSIONS

6.1 Summary

A multi-pronged investigation into the heating associated with some intravascular treatments was performed in the context of SMP devices actuated with fiber optics. Thermal energy is required to raise the polymer above its critical temperature, T_g, so that shape recovery can take place. A mock SMP device deployed inside of a human blood vessel was experimentally modeled as a simple metal cap on the tip of a hollow glass rod inserted and fiber optically actuated in a PDMS model of a long straight tube. Simulations corresponding to the simplified setup were run through a CFD package for comparison with PIV and LIF observations. Analytical solutions to the relevant simple cases of concentric annulus flow and straight pipe flow were also included.

Some key assumptions include steady laminar flow and internal forced convection heat transfer. Fluid properties were assumed constant and incompressible, though some temperature effects were discussed. Geometries, flow rates, fluid properties, and heat fluxes were matched as closely as possible between analyses.

Predictions were made from analytical solutions and simulations and then verified with the experimental techniques of PIV and LIF, showing quantitative agreement in the simplified baselines cases and qualitative similarity between the velocity and temperature distributions for the transition region.

6.2 Conclusions

In the context of laser-activated intravascular devices, especially those employing shape memory properties of SMP, the heat required for full device actuation is utmost important due to its possible detrimental effects on blood and vessel walls. The end goal of intravascular heating in SMP devices is full device actuation without damage to the patient. Optimal device heating exists at low flow rates and high input energy, in accordance with the literature [3], [5], [17]. Knowing that increased convective cooling caused by higher flow rates (and velocities) counteracts device actuation by carrying heat away from the SMP, it is reasonable to say that although a baffle or balloon blocking blood flow increases successful device actuation, the potential damage to the patient also increases.

This study has found that heating along the center axis of a tube carries the least threat of wall damage. The experimental fluid has similar properties to blood, but does not account for the non-Newtonian red blood cells, where thermal damage is likely. To this end, an Arrhenius damage integral taking into account the time of heating exposure is suggested for analysis of red blood cell damage.

The results show that PIV is an accurate tool for investigating SMP-based thermal actuation, where generic scenarios are consistent with theory and results are easily repeatable through robust algorithms. LIF has shown overall potential, but the technique is rather primitive and the undeveloped processing procedures rely heavily on high quality raw images. Before continuing more complex analyses with LIF, simple cases must be quantitatively confirmed as they were for PIV.

In the simplest case of an ideal cylindrical device in a perfectly straight artery, comparisons between analytical solutions, simulations, and experimentally derived quantities become relatively straightforward. These steps were necessary to ensure the PIV/LIF system can obtain results in agreement with theory. Future studies will extend the analysis to include more pertinent and complicated geometries, realistic devices composed of SMP, and unsteady flow rates. All of these additions make the analysis much more difficult, but the simple validations in this paper should lend promise to their accuracy.

REFERENCES

[1] W. Small IV, T.S. Wilson, P. Singhal, and D.J. Maitland, "Biomedical applications of thermally actuated shape memory polymers," *Journal of Materials Chemistry,* vol. 20, pp. 2256-2266, 2010.

[2] P.T. Mather, X. Luo, and I.A. Rousseau, "Shape memory polymer research," *Annual Review of Materials Research,* vol. 39, pp. 445-471, 2009.

[3] D.J. Maitland, W. Small IV, J.M. Ortega, P.R. Buckley, J. Rodriguez *et al.*, "Prototype laser-activated shape memory polymer foam device for embolic treatment of aneurysms," *Journal of Biomedical Optics,* vol. 12, no. 3, pp. 030504 (3 pages), 2007.

[4] J. Ortega, D. Maitland, T. Wilson, W. Tsai, O. Savas *et al.*, "Vascular dynamics of a shape memory polymer foam aneurysm treatment technique," *Annals of Biomedical Engineering,* vol. 35, no. 11, pp. 1870-1884, 2007.

[5] G.M. Baer, T.S. Wilson, W. Small IV, J. Hartman, W.J. Benett, D.L. Matthews, and D.J. Maitland, "Thermomechanical properties, collapse pressure, and expansion of shape memory polymer neurovascular stent prototypes," *Journal of Biomedical Materials Research Part B: Applied Biomaterials*, vol. 90B, pp. 421–429, 2009.

[6] B. Yang, W.M. Huang, C. Li, and L. Li, "Effects of moisture on the thermomechanical properties of a polyurethane shape memory polymer," *Polymer*, vol. 47, pp. 1348-56, 2006.

[7] M.Y. Yousif, D.W. Holdsworth, and T.L. Poepping, "Deriving a blood-mimicking fluid for particle image velocimetry and Sylgard-184 vascular models," 31st Annual International Conference of the IEEE EMBS. Minneapolis, Minnesota: September, 2009.

[8] T. Pfefer, B. Choi, G. Vargas, K.M. McNally, and A.J. Welch, "Pulsed laser-induced thermal damage in whole blood," *Transactions of ASME*, vol. 122, pp. 196-202, 2000.

[9] J. Pearce and S. Thomsen, "Rate process analysis of thermal damage," Chap. 17 in *Optical-Thermal Response of Laser-Irradiated Tissue*, A.J. Welch, MJC van Gemert, editors. New York: Plenum Press, pp. 160-162, 1995.

[10] G.J. Monkman, "Advances in shape memory polymer actuation," *Mechatronics*, vol. 10, pp. 489-498, 2000.

[11] G.M. Baer, W. Small IV, T.S. Wilson, W.J. Benett, D.L. Matthews, J. Hartman, and D.J. Maitland, "Fabrication and *in vitro* deployment of a laser-activated shape memory polymer vascular stent," *Biomedical Engineering Online*, vol. 6, November, 2007.

[12] W. Small IV, M.F. Metzger, T.S. Wilson, and D.J. Maitland, "Laser-activated shape memory polymer microactuator for thrombus removal following ischemic stroke: preliminary *in vitro* analysis," *IEEE Journal of Selected Topics in Quantum Electronics*, vol. 11, July/August, 2005.

[13] W. Small IV, E. Gjersing, J.L. Herberg, T.S. Wilson, and D.J. Maitland, "Magnetic resonance flow velocity and temperature mapping of a shape memory polymer foam device," *Biomedical Engineering Online.* vol. 8, December, 2009.

[14] P.R. Buckley, G.H. McKinley, T.S. Wilson, W. Small IV, W.J. Benett *et al.*, "Inductively heated shape memory polymer for the magnetic actuation of medical devices," *IEEE Transactions on Biomedical Engineering*, vol. 53, pp. 2075-2083, October, 2006.

[15] E.K. Hahn, "Preliminary investigation of heat transport phenomena during SMP foam actuation", final paper for Undergraduate Summer Research Grant program, Texas A&M University, 2009.

[16] W. Tsai, O. Savas, D. Maitland, J. Ortega, W. Small IV *et al.*, "Experimental study of the vascular dynamics of a saccular basilar aneurysm," Proceedings of 2006 ASME International Mechanical Engineering Congress and Exposition, vol. 262, pp. 317-326, November, 2006.

[17] M.D. Ford, H. N. Nikolov, J. S. Milner, S. P. Lownie, E. M. DeMont *et al*., "PIV-measured versus CFD-predicted flow dynamics in anatomically realistic cerebral aneurysm models," *Journal of Biomechanical Engineering*, vol. 130, pp. 012125-1 (9 pages), 2008.

[18] S.C.M. Yu, "Steady and pulsatile flow studies in abdominal aortic aneurysm models using particle image velocimetry," *International Journal of Heat and Fluid Flow*, vol. 21, pp. 74-83, 2000.

[19] C.N. Ionita, Y. Hoi, H. Meng, and S. Rudin, "Particle image velocimetry (PIV) evaluation of flow modification in aneurysm phantoms using asymmetric stents," Proc. SPIE 5369. pp. 295-306, Feburary, 2004.

[20] H. Hui and M.K. Manoochehr, "Molecular tagging velocimetry and thermometry and its application to the wake of a heated circular cylinder," *Measurement Science and Technology*, vol. 17, p. 1269, 2006.

[21] H.J. Seuntiens, R.N. Kieft, C.C.M. Rindt, and A.A. van Steenhoven, "2D temperature measurements in the wake of a heated cylinder using LIF," *Experiments in Fluids*, vol. 31, pp. 588-595, 2001.

[22] J. Sakakibara and R.J. Adrian, "Whole field measurement of temperature in water using two-color laser induced fluorescence," *Experiments in Fluid,* vol. 26, pp. 7-15, 1999.

[23] M.C.J. Coolen, R.N. Kieft, C.C.M. Rindt, and A.A. van Steenhoven, "Application of 2-D LIF temperature measurements in water using a Nd:YAG laser," *Experiments in Fluids*, vol. 27, pp. 420-426, 1999.

[24] L. Baranyi, S. Szabó, B. Bolló, and R. Bordás, "Analysis of low Reynolds number flow around a heated circular cylinder," *Journal of Mechanical Science and Technology*, vol. 23, pp. 1829-1834, 2009.

[25] M. Raffel, C. Willert, S. Wereley, and J. Kompenhans, *Particle Image Velocimetry, a Practical Guide*, 2nd ed., Berlin: Springer, 2007.

[26] L. Parlea, R. Fahrig, D.W. Holdsworth, and S.P. Lownie, "An analysis of the geometry of saccular intracranial aneurysms," *American Journal of Neuroradiology*, vol. 20, pp. 1079-1089, 1999.

[27] E.R. Kandel, J.H. Schwartz, and T.M. Jessell, *Principles of Neural Science*. Ed. 4, McGraw-Hill: 2000

[28] H. Lamb, *Hydrodynamics,* Cambridge University Press: London, 1924.

[29] R.K. Shah and A.L. London, *Laminar Flow Forced Convection in Ducts: A Source Book for Compact Heat Exchanger Analytical Data*, Academic Press: New York, 1978.

[30] R.E. Lundberg, P.A. McCuen, and W.C. Reynolds, "Heat transfer in annular passages: hydrodynamically developed laminar flow with arbitrarily prescribed wall temperatures and heat fluxes," *Int. J. Heat Mass Transfer*, vol. 6, pp. 495-529, 1962.

[31] R.E. Lundberg, W.C. Reynolds, and W.M. Kays, "Heat transfer with laminar flow in concentric annuli with constant and variable wall temperature and heat flux," Thermosciences Division, Dept. Mech. Engineering, Report AHT-2, Stanford University, 1961.

[32] P.M. Worsoe-Schmidt, "Heat transfer in the thermal entrance region of circular tubes and annular passages with fully developed laminar flow," *Int. J. Heat Mass Tranfer*, vol. 10, pp. 541-551, 1967.

[33] M. Jakob and K.A. Rees, “Heat transfer to a fluid in laminar flow through an annular space,” *Trans AIChE*, vol. 37, pp. 619-648, 1941.

[34] A.P. Hatton and A. Quarmby, “Heat transfer in the thermal entry length with laminar flow in an annulus, *Int. J. Heat Mass Transfer*, vol. 5, pg. 973, 1962.

[35] S.F. Chien, “Heat transfer from a short heated section in annular flow,” *Int. J. Heat Mass Transfer*, vol. 12, pp. 31-43, 1969.

[36] M.A. Ebadian and Z.F. Dong, Chapter Five: Forced Convection, Internal Flow in Ducts, in W.M. Rohsenow, J.P. Hartnett, and Y.I. Cho, *Handbook of Heat Transfer*, 3rd ed., 1998.

[37] N.G. Kafoussias and E.W. Williams, “The effect of temperature-dependent viscosity on free-forced convective laminar boundary layer flow past a vertical isothermal flat plate,” *Acta Mechanics*, vol. 110, pp. 123-137, 1995.

APPENDIX A

Clarification of Nomenclature Scheme

In compiling heat exchanger data, Shah and London adopt the convention of Kays *et al.* recommended for doubly connected heat transfer problems in ducts. Since they consider all possible cases for concentric annuli, they found it necessary to include a parenthesized superscript, i.e. (k=1, 2, 3, 4) for every temperature distribution and Nusselt number, to indicate which of the four fundamental solutions they correspond to. In this thesis, only fundamental solutions of the second kind (k=2, constant heat flux at one wall with adiabatic opposite wall) are considered and the superscript notation is unnecessary. The subscript notation, however, is still a little bit confusing and clarification is in order.

For general quantities with a single subscript, such as dimensionless temperature θ_j, the subscript *j* refers to the heated wall. In this study, only the inner wall is heated so $(j = i)$ in all cases.

For quantities with multiple subscripts, such as $Nu_{x,lj}$, $Nu_{m,lj}$, or Nu_{lj}, the first subscript (x or m) represents the local (x) or mean (m) value in the thermal entrance region. After the comma, subscript *l* refers to the wall at which the quantity is evaluated ($l = i$ or o) and the last subscript *j* still refers to the heated wall as it did above $(j = i)$. The last example above (only two subscripts) denotes the peripheral average Nusselt number for the fully developed region. This notation also applies to dimensionless temperatures $\theta_{x,lj}$, $\theta_{m,lj}$, or θ_{lj}.

APPENDIX B

Concentric Annulus Solutions to Conservation Equations

B.1 Hydrodynamically and Thermally Fully Developed

Jakob & Rees begin with the CONVECTIVE part, where the velocity profile (B.1) is as given and (B.2) is converted to the current notation.

$$u = -\frac{1}{4\mu}\frac{dP}{dx}\left(r_i^2 - r^2 + \bar{B}\ln\frac{r}{r_i}\right) \tag{B.1}$$

$$u = -\frac{1}{4\mu}\frac{dP}{dx}r_o^2\left(r^{*2} - \bar{r}^2 + B\ln\frac{r}{r_i}\right) \tag{B.2}$$

The conversion of constants can be found by $\bar{B} = \frac{r_o^2 - r_i^2}{\ln\frac{r_o}{r_i}} = r_o^2 B$. The bar above the constant distinguishes it from constants used in later papers (e.g. Lundberg *et al.* and Worsoe-Schmidt) as well as this thesis The volume flow rate is then found from integration

$$\int_0^Q dQ = \int_{r_i}^{r_o} u \cdot 2\pi r \cdot dr \tag{B.3}$$

$$Q = -\frac{\pi}{8\mu}\bar{M}\frac{dP}{dx}, \quad where\ \bar{M} = (r_o^2 - r_i^2)(r_o^2 + r_i^2 - \bar{B}) \tag{B.4}$$

The heat picked up in unit time by the fluid on its way through the differential ring,

$$dq_{conv} = \rho C_P \cdot dQ\frac{\partial T}{\partial x}dx = \rho C_P \cdot u \cdot 2\pi r \cdot dr\frac{\partial T}{\partial x}dx \tag{B.5}$$

Now, the CONDUCTIVE part, consisting of radial and axial heat gain

$$dq_{cond,rad} = 2\pi k\left[\frac{\partial}{\partial r}\left(r\frac{\partial T}{\partial r}\right)\right]dr \cdot dx \tag{B.6}$$

$$dq_{cond,axial} = 2\pi kr \cdot dr\frac{\partial^2 T}{\partial x^2} \cdot dx \tag{B.7}$$

The above three (B.5 – B.7) are plugged into the heat balance (B.8) below

$$dq_{conv} = dq_{cond,rad} + dq_{cond,axial} \tag{B.8}$$

leading to the general differential equation for annulus heat flow, after some substitution and simplification,

$$\frac{\partial}{\partial r}\left(r\frac{\partial T}{\partial r}\right) = \bar{N}r\left(r_i^2 - r^2 + \bar{B}\ln\frac{r}{r_i}\right)\frac{\partial T}{\partial x} - r\frac{\partial^2 T}{\partial x^2},\ where\ \bar{N} = \frac{2Q\rho C_P}{\pi Mk} = const \tag{B.9}$$

Assume uniform heating such that $\frac{\partial T}{\partial x} = C = const$ and $\frac{\partial^2 T}{\partial x^2} = 0$, above reduces to:

$$\frac{d}{dr}\left(r\frac{dT}{dr}\right) = \bar{N}C\left(r_1^2 r - r^3 + \bar{B}r\ln\frac{r}{r_i}\right) \tag{B.10}$$

Defining $\theta = T - T_i$, integrating twice, and solving for the constants of integration with the boundary conditions $\left(\frac{d\theta}{dr} = 0\ at\ r = r_o, and\ \theta = 0\ at\ r = r_i\right)$ leads to the temperature distribution,

$$\theta = \bar{N}C\left[\frac{r^2}{4}\left(r_i^2 - \frac{r^2}{4} + \bar{B}\ln\frac{r}{r_i} - \bar{B}\right) + \frac{r_o^2}{4}(r_o^2 - \bar{B})\ln\frac{r}{r_i} - \frac{r_i^2}{4}\left(\frac{3r_i^2}{4} - \bar{B}\right)\right]$$

$$= \bar{N}C \cdot \psi(r) \tag{B.11}$$

$$\frac{d\theta}{dr} = \bar{N}C\left[\frac{r}{2}\left(r_i^2 - \frac{r^2}{2} + \bar{B}\ln\frac{r}{r_i} - \frac{B}{2}\right) - \frac{r_o^2}{4r}(r_o^2 - \bar{B})\right]$$

$$= \bar{N}C \cdot \psi'(r) \tag{B.12}$$

where $\bar{N}$ is defined in (B.9) and $\psi(r)$ and $\psi'(r)$ represent the radial dependent quantity in brackets. The heat gain through the wall of tube T_i for length Δx is found to be

$$q_1 = -k \cdot 2\pi r_i \left(\frac{d\theta}{dr}\right)_{r=r_i} \Delta x = -k \cdot 2\pi r_i \cdot \Delta x \cdot NC \cdot \psi'(r)_{r=r_i} \tag{B.13}$$

Equating (B.13) and the definition of a surface heat transfer coefficient, $q_1 = h_{12} \cdot \Delta x \cdot 2\pi r_i(T_i - T_o)$, the heat transfer coefficient is found to be, since $\psi(r)_{r=r_i} = 0$,

$$h_{io} = -\frac{k\cdot\psi'(r)_{r=r_i}}{\psi(r)_{r=r_i}-\psi(r)_{r=r_o}} = \frac{k\cdot\psi'(r)_{r=r_i}}{\psi(r)_{r=r_o}} \tag{B.14}$$

For a DIMENSIONLESS REPRESENTATION of one sided heating, (B.14) can be transformed into

$$\frac{h_{12}r_i}{k} = y\frac{\psi'(y)}{\psi(y)} = \frac{\Phi'(y)}{\psi(y)},\ since\ \psi'(y) = -\frac{1}{y}\Phi'(y) \tag{B.15}$$

where the left side is a Nusselt dimensionless group, and the right side is a function of radius ratio, r^*, only. They also note that it is more customary to use the mean mixing temperature of the fluid rather than T_o and T_i to define a heat transfer coefficient.

$$\theta_m = \frac{\int_{r_i}^{r_o} u\cdot 2\pi r\cdot\theta\cdot dr}{\int_{r_i}^{r_o} u\cdot 2\pi r\cdot dr} = \frac{NC\int_{r_i}^{r_o} u\cdot 2\pi r\cdot\varphi(r)\cdot dr}{\int_{r_i}^{r_o} u\cdot 2\pi r\cdot dr} \tag{B.16}$$

B.2 Hydrodynamically Developed, Thermally Developing

When the thermal fields are not fully developed , Shah and London combined the results of two main approaches, namely the eigenvalue solution of Lundberg *et al.* for $x^* > 10^{-2}$ and the Leveque-type solution of Worsoe-Schmidt for $x^* < 10^{-2}$. They briefly mention the agreement of Hatton and Quarmby's results with those of Lundberg et al. The relevant approaches are summarized below.

Hatton & Quarmby made use of the following dimensionless parameters:

$$R = \frac{r}{r_o - r_i} = \frac{2r}{D_h}, \qquad L = \frac{4}{Re\cdot Pr}\left(\frac{x}{D}\right), \qquad Re = \frac{u_m D_h}{\nu}$$

Velocity profile for an annulus is given as,

$$\bar{u} = \frac{2\left(R_o^2 - R_i^2 - 2R_{max}^2\ln R_o/R_i\right)}{R_o^2 + R_i^2 - 2R_{max}^2},\ where\ R_{max}^2 = \frac{R_o^2 - R_i^2}{2\ln R_o/R_i} \tag{B.17}$$

The energy equation becomes:

$$\rho \cdot C_P \cdot u \frac{\partial T}{\partial x} = \frac{1}{r}\frac{\partial}{\partial r}\left(\alpha \cdot r \frac{\partial T}{\partial r}\right) \tag{B.18}$$

Bulk mean temperature and dimensionless temperature are defined,

$$T_m = \frac{\int_{r_i}^{r_o} u \cdot T \cdot 2\pi r \cdot dr}{u_m \pi (r_o^2 - r_i^2)} = \frac{2}{2R_i + 1}\int_{R_i}^{R_o} U \cdot T \cdot R \cdot dR \tag{B.19}$$

$$\theta = \frac{T - T_e}{qD_h/_k} \tag{B.20}$$

The usual procedure for direction integration, e.g. Sparrow *et al.*, divides the solution into two parts, θ_1 the fully developed solution, and θ_2 an entry temperature which disappears at large L.

$$\theta_1 = \frac{R_i L}{2R_i + 1} + G_{fd} \tag{B.21}$$

where $G_{fd} = f(R)$, representing the fully developed solution with bulk mean value of 0.

$$\theta_2 = \sum_{n=0}^{\infty} C_n Y_n \cdot \exp(-\lambda_n^2 L) \tag{B.22}$$

where λ_n and Y_n are eigenvalues and functions of

$$\frac{d^2 Y}{dR^2} + \frac{1}{R}\frac{dY}{dR} + \lambda^2 UY = 0 \tag{B.23}$$

with boundary conditions: $\frac{dY}{dR} = 0,\ at\ R = R_i\ and\ R = R_o$

Constant can be found, $C_n = -\frac{\int_R^{R_o} R \cdot U \cdot G \cdot Y_n dR}{\int_{R_i}^{R_o} R \cdot U \cdot Y_n^2 dR}$, and finally the Nusselt number becomes

$$Nu = \frac{1}{G_i\left[1 - \sum_{n=0}^{\infty} C_n \exp(-\lambda_n^2 L)\right]} \tag{B.24}$$

Lundberg, McCuen, & Reynolds

Note $\bar{x} = x^*$ in the following sections. Equation for temperature field,

$$\frac{\partial^2\theta}{\partial\bar{r}^2} + \frac{1}{\bar{r}}\frac{\partial\theta}{\partial\bar{r}} = \frac{U(\bar{r})}{n}\frac{\partial\theta}{\partial\bar{x}} \tag{B.25}$$

where $$u(\bar{r}) = \frac{2u_m}{M}(1 - \bar{r}^2 + B\ln\bar{r}) \tag{B.26}$$

For LARGE $\bar{x}$, the fundamental boundary conditions can be made homogeneous by subtracting the fully developed solution, i.e. solutions valid as $\bar{x}$ tends to infinity. Let $\bar{\theta}_j = \theta_j - \theta_{j,fd}$ and the boundary conditions for the second kind are

$$\frac{\partial\bar{\theta}_i}{\partial\bar{r}} = 0, \qquad at\ \bar{r} = r^*\ and\ 1, \qquad for\ all\ x$$

$$\bar{\theta}_i(\bar{r}, o) = -\frac{r^*}{1+r^*}\frac{1}{M(1-r^*)^2}\left[\frac{1-B}{2}(\bar{r}^2 - \ln\bar{r}) - \frac{\bar{r}^4}{8} + \frac{B}{2}\bar{r}^2\ln\bar{r} - \frac{(r^*)^2M}{2}\right.$$

$$\left. + \frac{1+\ln r^*}{2} + \frac{(r^*)^4}{8}\right] - [\theta_{ii} - \theta_{mi}]_{fd}$$

$$\frac{\partial\bar{\theta}_o}{\partial\bar{r}} = 0, \qquad at\ \bar{r} = r^*\ and\ 1, \qquad for\ all\ \bar{x}$$

$$\bar{\theta}_o(\bar{r}, o) = \frac{1}{(1+r^*)M(1-r^*)}\frac{1-B}{2}(\bar{r}^2 - 1) - \frac{(\bar{r}^4 - 1)}{8} + \frac{B}{2}\bar{r}^2\ln\bar{r}$$

$$- \frac{(r^*)^2}{2}[(r^*)^2 - B]\ln\bar{r} - [\theta_{oo} - \theta_{mo}]_{fd}$$

For SMALL values of $\bar{x}$, the energy equation can be reduced by neglecting the curvature of the velocity profile and approximating it by a linear equation using the wall slope of the actual velocity, known as the Leveque approximation. The reduced equation, when the nonzero (heating) boundary condition is applied at the inner wall, is

$$\frac{\partial^2\theta}{\partial\bar{r}^2} = E_i(\bar{r} - r^*)\frac{\partial\theta}{\partial\bar{x}} \tag{B.27}$$

For fundamental solutions of the second and fourth kinds, set $\theta = \bar{x}^{1/3} f(p)$, where $p = (\bar{r} - r^*)/\bar{x}^{1/3}$ or $p = (\bar{r} - 1)/\bar{x}^{1/3}$., which results in

$$\theta_{ii} = \frac{0.36925}{(1-r^*)} \left[\frac{(B/r^*)-2r^*}{18(1-r^*)^2 M}\right]^{-1/3} \bar{x}^{1/3} \tag{B.28}$$

where $\theta_{ii} = \hat{C}_{ij} \bar{x}^{1/3}$. The complete equation can be solved by separation of variables, giving

$$\theta_j = \left(\theta_j\right)_{fd} + \sum_{n=0}^{?} (C_n)_j R_n^{(k)} \exp(-\lambda_n^2 \bar{x}) \tag{B.29}$$

where $R_n^{(k)}$ satisfies the Sturm-Liouville equation

$$\frac{d^2 R_n^{(k)}}{d\bar{r}^2} + \frac{1}{\bar{r}} \frac{dR_n^{(k)}}{d\bar{r}} + \lambda_n^2 N(1 - \bar{r}^2 + B \ln \bar{r}) R_n^{(k)} = 0 \tag{B.30}$$

The λ_n, n=0,1 ,2, comprise an infinite set of eigenvalues for which $R_n^{(k)}$ will satisfy the boundary conditions at $\bar{r} = r^* \; and \; 1$ as specified for the solutions of the *k*th kind. The coefficients of the series are given by

$$(C_n)_j = \frac{\int_{r^*}^{1} w(\bar{r}) \theta_{j_{fd}} R_n^{(k)} d\bar{r}}{\int_{r^*}^{1} w(\bar{r}) \left[R_n^{(k)}\right]^2 d\bar{r}} \tag{B.31}$$

where $w(\bar{r}) = N(\bar{r} - \bar{r}^3 + B\bar{r} \ln \bar{r})$

Now the various fundamental solutions can be constructed from (B.29) and the various non-dimensional quantities can be evaluated as functions of the axial position parameter, $\bar{x}$. The θ_{ij} can be evaluated directly from (20) and we have, additionally, the relations

$$\Phi_{ij} = -2(1 - r^*) \left[\frac{\partial \theta_j}{\partial \bar{r}}\right]_{\bar{r}=r^*} \tag{B.32}$$

$$\Phi_{oj} = 2(1 - r^*) \left[\frac{\partial \theta_j}{\partial \bar{r}}\right]_{\bar{r}=1} \tag{B.33}$$

$$\theta_{mj} = \frac{4}{1+r^*}\int_o^{\bar{x}}\left[r^*\Phi_{ij} + \Phi_{oj}\right]d\bar{x} \tag{B.34}$$

related to the conventional Nusselt modulus by,

$$Nu_{lj} = \frac{\Phi_{lj}}{[\theta_{lj}-\theta_{mj}]} \tag{B.35}$$

Worsoe-Schmidt

Energy equation given as

$$u(r)T_x = \frac{\alpha}{r}(rT_r)_r, \;\; or \;\; u\frac{\partial T}{\partial x} = \frac{\alpha}{r}\left(r\frac{\partial T}{\partial r}\right) \tag{B.36}$$

with $T(0,r) = T_e, \quad r_i \le r \le r_o$

For solutions of the second kind (step heat flux at r_i, adiabatic at r_o), and $x>0$, boundary conditions given as

$$T_r(r_j, x) = sq"_j/k$$

$$T_r(r_k, x) = 0$$

With dimensionless variables, energy equation becomes,

$$\bar{u}\bar{T}_{\bar{x}} = \bar{T}_{\bar{y}\bar{y}} + \frac{R}{1+R\bar{y}}\bar{T}_{\bar{y}} \tag{B.37}$$

Introducing similarity variables from the Leveque solution (ξ, η), and a dimensionless temperature function, $\theta(\xi,\eta), where\ \theta = \bar{T}/\xi$ for solutions of the second kind,

$$\eta = \bar{y}/\xi\,, \qquad where\ \xi = (9\bar{x}/A)^{\frac{1}{3}}$$

$$\theta(\xi,\eta) = \sum_{n=0}^{\infty}\xi^n\theta_n(\eta) \tag{B.38}$$

The above expression, along with the previous velocity profile expansion (12), letting $\bar{y} = \xi\eta$, and equating like powers of ξ leads to the following ODE system:

$$\theta''_o + 3\eta^2\theta'_o - 3p\eta\theta_o = 0 \tag{B.39}$$

$$\theta''_n + 3\eta^2\theta'_n - 3(n+1)\eta\theta_n$$

$$= \sum_{m=1}^{n} \{[(-R)^m - 3a_m\eta^3]\eta^{m-1}\theta'_{n-m} + 3(n-m+1)a_m\eta^{m+1}\theta_{n-m}\}$$

$$n = 1, 2, \ldots \tag{B.40}$$

Boundary conditions for solutions of the second kind,

$$\theta'_o(0) = -1; \quad \theta_o(\infty) = 0$$

$$\theta'_n(0) = 0; \quad \theta_n(\infty) = 0$$

As long as $\xi\eta_{max} \leq 1$, an adiabatic condition is enforced on the opposite wall and determines the maximum $\bar{x}$ for which the solution is valid: $\bar{x} = A/9\eta_{max}^3$. For annuli with the inner wall heated and $r^* \geq 0.5$, values of $\bar{x}$ lie above values for the flat duct. If, however, $r^* \leq 0.5$, a more restrictive condition follows from the power series expansion of the velocity profile, namely $R\bar{y} < 1$, giving

$$\bar{x}_{max} = \frac{r^*}{1-r^*}\frac{A}{9\eta_{max}^3} \tag{B.41}$$

For a step-change in wall temperature (p=0), the solution of the unperturbed equation (B.39) is the well-known Leveque solution (not shown here). The corresponding solution for uniform heat flux (p=1) is

$$\theta_o = \frac{2}{3\Gamma\left(\frac{5}{3}\right)}e^{-\eta^3} - \eta\left[1 - \frac{2}{\Gamma\left(\frac{5}{3}\right)}\int_0^\eta \mu e^{-\mu^3}d\mu\right] \tag{B.42}$$

Where tabulated results show $\theta_o(0) = 0.73849$.

For the inverse problem of the second kind; namely, “given the heat flux, what is the temperature?”, the non-dimensional wall temperature to the Nth approx,

$$\bar{T}_j^{(2)} = \sum_{n=0}^{N} \left(\frac{9\bar{x}}{A}\right)^{(n+1)/3} \theta_{j,n}^{(2)}(0) \tag{B.43}$$

The mixed mean temperature, from an energy balance over the duct length $\bar{x}$,

$$\bar{T}_{m,j}^{(2)} = \frac{2\bar{r}_j}{1+r^*}\bar{x} \tag{B.44}$$

And the Nusselt numbers,

$$Nu_j^{(2)} = \frac{2}{\left(\bar{T}_j - \bar{T}_{m,j}^{(2)}\right)} \tag{B.45}$$

Results are more accurate with smaller $\bar{x}$. Higher order solutions are generally well behaved in that neither the functions nor their derivatives increase significantly in magnitude with increasing order, except for a less satisfactory behavior with the inner wall heated when r* is less than 0.5. As r* decreases, the higher order functions increase rapidly and series convergence becomes increasingly slow. And since the range of $\bar{x}$ in which the solutions are valid decreases as $r^*/(1-r^*)$, solutions with heating at the inner wall only given for $r^* \geq 0.1$.

Worsoe-Schmidt also included Nusselt number comparisons with Lundberg *et al.* (1963) for annular passage and flat duct solutions, Munakata (1962) for step-change in wall temperature in a circular tube (eigenfunctions computed by Brown (1960)), and Sellars *et al*. (1956) for step-change in heat flux in a circular tube from their eigenvalues and related constants. Agreement is excellent in the downstream portions of range.

VITA

Name:	Casey David McCurrin
Address:	Department of Biomedical Engineering 5045 Emerging Technologies Bldg College Station, TX 77843-3120
Email Address:	cmccurrin@tamu.edu
Education:	B.S., Electrical Engineering, Texas A&M University, 2009 M.S., Biomedical Engineering, Texas A&M University, 2012